Eur. J. Mineral., 32, 557–574, 2020
https://doi.org/10.5194/ejm-32-557-2020

European Journal of Mineralogy
Open Access

Two new minerals, badengzhuite, TiP, and zhiqinite, $TiSi_2$, from the Cr-11 chromitite orebody, Luobusa ophiolite, Tibet, China: is this evidence for super-reduced mantle-derived fluids?

Fahui Xiong[1,2], Xiangzhen Xu[1], Enrico Mugnaioli[3], Mauro Gemmi[3], Richard Wirth[4], Edward S. Grew[5], Paul T. Robinson[1], and Jingsui Yang[1,2,6]

[1]Center for Advanced Research on the Mantle (CARMA), Key Laboratory of Deep-Earth Dynamics of Ministry of Land and Resources, Institute of Geology, Chinese Academy of Geological Sciences, Beijing, 100037, China
[2]Southern Marine Science and Engineering Guangdong Laboratory (Guangzhou), Guangzhou, 511458, China
[3]Center for Nanotechnology Innovation@NEST, Istituto Italiano di Tecnologia (IIT), Piazza San Silvestro 12, 56127 Pisa, Italy
[4]Helmholtz Centre Potsdam, GFZ German Research Centre for Geosciences, Section 3.5, Interface Surface Geochemistry, Telegrafenberg, C 120, 14473 Potsdam, Germany
[5]School of Earth and Climate Sciences, University of Maine, Orono, Maine 04469, USA
[6]School of Earth Sciences and Engineering, Nanjing University, Nanjing, 210023, China
Correspondence: Edward S. Grew (esgrew@maine.edu)

Received: 27 June 2020 – Revised: 25 August 2020 – Accepted: 8 October 2020 – Published: 2 November 2020

Abstract. Titanium minerals enclosed in corundum separated from the Cr-11 orebody include native Ti, zamboite ($FeTiSi_2$), osbornite (TiN)-khamrabaevite (TiC) solid solutions, and jingsuiite (TiB_2), as well as the new minerals badengzhuite (TiP) and zhiqinite ($TiSi_2$) and two potentially new minerals, $Ti_{11}(Si,P)_{10}$ and $Ti_{10}(Si,P,\square)_7$, where $\square$ indicates a vacancy. These minerals together constitute a spheroid 20 µm across inferred to have crystallized from a droplet of Ti–Si–P intermetallic melt. Energy-dispersive spectroscopy and three-dimensional electron diffraction were applied to characterize the two new minerals. Badengzhuite has a primitive hexagonal cell with $a = 3.49(7)$ Å, $c = 11.70(23)$ Å, $V = 124(4)$ Å^3, and crystallizes in space group $P6_3/mmc$ ($Z = 4$). It is isostructural with synthetic TiP. Two EDX (energy dispersive X-ray spectroscopy) analyses of badengzhuite gave 60.56 wt %Ti and 39.44 wt % P and 62.74 wt % Ti and 37.26 wt % P from which an empirical formula of $Ti_{1.020}P_{0.980}$ was calculated on the basis of two atoms (ideally TiP). Zhiqinite has a primitive orthorhombic cell with $a = 8.18(16)$ Å, $b = 4.85(10)$ Å, $c = 8.42(17)$ Å, $V = 334(12)$ Å^3, and crystallizes in space group $Fddd$ ($Z = 8$). It is isostructural with synthetic $TiSi_2$ (C54 type). Four EDX analyses of zhiqinite gave 39.58–44.79 wt % Ti and 55.21–60.42 wt % Si, from which an empirical formula of $Ti_{0.905}Si_{2.095}$ was calculated on the basis of three atoms (ideally $TiSi_2$). We suggest that interaction of mantle-derived $CH_4 + H_2$ fluids with basaltic magmas in the shallow lithosphere (depths of ~ 30–100 km) under conditions more reducing than 6 log units below the oxygen fugacities corresponding to the iron–wüstite buffer resulted in precipitation of corundum that entrapped intermetallic melts, some of which crystallized to ultra-reduced Ti–P–Si phases. Experimental work on the Ti–Si and Ti–P systems indicates that the minerals enclosed in corundum could have crystallized from the alloy melt at the lowest temperature accessible on the liquidus. It has been alleged that these ultra-reduced phases are anthropogenic contaminants inadvertently introduced with fused alumina abrasive during preparation of mineral separates. Nonetheless, we conclude that the differences between the ultra-reduced minerals in the separates and the ultra-reduced phases in fused alumina are more convincing evidence for these minerals having a natural origin than the similarities between them are evidence for an anthropogenic origin.

1 Introduction

Chromitite orebodies in the Luobusa ophiolite have yielded a great variety of minerals for which the most prolific has been the Cr-31 chromitite orebody near Luobusa and the Cr-11 chromitite orebody near Kangjinla (Fig. 1, Table 1), which are located about 11 km apart in harzburgite near the contact with the transition zone dunite. Minerals separated from the Cr-31 chromitite include the ultrahigh-pressure (UHP) minerals diamond, moissanite, and coesite pseudomorphs of stishovite, as well as several new super-reduced species such as linzhiite, $FeSi_2$ (Li et al., 2012); titanium, Ti (Fang et al., 2013); zangboite, $TiFeSi_2$ (Li et al., 2009); and qingsongite (cubic BN) (Dobrzhinetskaya et al., 2009, 2014). Super-reduced intermetallic phases have also been found in the Cr-11 podiform chromitite orebody in the Luobusa ophiolite (Table 1, Fig. S1), which is located at 29°11′ N, 92°18′ E with an elevation of 5300 m in the Kangjinla district. However, the mode of occurrence is very different – the phases are enclosed in corundum grains (Fig. S2a) extracted from the Cr-11 chromitite. Xu et al. (2009, 2013, 2018) reported compounds that appear to correspond to known minerals, such as native titanium (Fang et al., 2013), Ti–Fe–Si (probably zangboite, $FeTiSi_2$, Li et al., 2009), Ti–N (osbornite), and Ti–C (khamrabaevite), as well as several Ti–Si, Ti–Si–P, and Ti–B intermetallic phases.

Our studies using three-dimensional electron diffraction (3D ED) have not only confirmed the identity of TiN and TiC intermetallic compounds as osbornite-khamrabaevite solid solutions, but they also revealed the identity of five intermetallic compounds as distinct minerals with the compositions TiB_2, TiP, $TiSi_2$, $Ti_{10}(Si,P,\square)_7$, and $Ti_{11}(Si,P)_{10}$ (Xiong et al., 2019a, b). The first three have been approved by the International Mineralogical Association's Commission on New Minerals, Nomenclature and Classification (IMA CNMNC) as new minerals: jingsuiite (Xiong et al., 2019b, 2020c), badengzhuite (Xiong et al., 2019c, this paper), and zhiqinite (Xiong et al., 2019d, this paper). A compound analyzed as TiP but without crystallographic data has been reported from a fulgurite (Essene and Fisher, 1986; Hawthorne et al., 1988), whereas $TiSi_2$ has yet to be reported in nature. Badengzhuite and zhiqinite have been synthesized but largely at atmospheric pressure (e.g., Nowotny, 1963; Snell, 1967, Okamoto, 2007; Fiore et al., 2016). Nonetheless, Li et al. (2013) reported the synthesis of $TiSi_2$ at high pressure; thus, there is no reason why TiP and the other three new minerals could not have formed at the higher pressures implied by the presence of diamond recovered from the Cr-11 orebody (Xu et al., 2009, 2015). Compositions of four of the new intermetallic compounds, including badengzhuite and zhiqinite, lie in the Ti–Si–P system and thus provide new information on this little-studied ternary system, which is information that can add a valuable perspective for understanding the conditions under which the Luobusa ophiolite was exhumed following burial to the upper mantle.

2 Mineral name and deposition of holotype material

The new mineral and its name, badengzhuite, was approved by the IMA CNMNC (IMA2019-076) (Xiong et al., 2019c). The mineral is named for Tibetan geologist Badengzhu (born 28 January 1939) of the Tibet Ore Industry Co., Ltd., Lhasa. In the literature, his name is sometimes written with "Ba" as his surname and "Dengzhu" as his given name. He discovered the chromite ore bodies in the Luobusa ophiolite in 1966 and is co-author of about 21 papers and two Chinese geologic books. He presided over the preliminary investigation of ophiolite and chromite in the Yarlung Zangbo suture zone in Tibet and completed in 1992–1998 both the Luobusa ophiolitic geological map at 1 : 50 000 and the Zedong ophiolitic geological map at 1 : 50 000. Starting from 2012, he presided over the deep prospecting work of Luobusa, discovered the Cr-80 ore body, and increased the reserves of chromite ore by 2.2×10^6 t.

Zhiqinite was approved by the IMA CNMNC (IMA2019-077) (Xiong et al., 2019d). Xu Zhiqin, a structural geologist, was born in Shanghai in 1941. In 1958, she was admitted to the Department of Geology of Peking University. She graduated in 1964 and was assigned to the Institute of Geology of the Chinese Academy of Geological Sciences in the same year. In the early 1980s, she went to the University of Montpellier in France to study. In 1987, she received her PhD in geology from the University of Montpellier. She served as deputy dean of the Chinese Academy of Geological Sciences and director of the Institute of Geology. In 1995, she was elected as an academician of the Chinese Academy of Sciences. Under the leadership of Xu Zhiqin, the scientific research group established the "Continental Dynamics Key Laboratory" of the Ministry of Land and Resources and discovered a large number of deep mantle minerals.

The holotype specimen of both badengzhuite and zhiqinite has been submitted to the Chinese Geological Museum, Xisiyangrouhutong 15th, Xicheng District, Beijing, China. The number assigned to this specimen is M13817 (source of foil no. 5358). Foil no. 5358 is to be kept with the specimens in the Chinese Geological Museum.

3 Geological background

The Yarlung Zangbo suture zone extends more than 2000 km longitudinally in southern Tibet and marks the boundary between the Indian subcontinent and Eurasia. The Luobusa ophiolite, located about 200 km east-southeast of Lhasa (Fig. 1), is the only body that contains significant chromitite deposits. It extends ∼ 43 km east–west and has a maximum

Table 1. Minerals found in chromitites in the Luobusa ophiolite compared to minerals from Mount Carmel, Israel, and compounds in fused alumina abrasive. Note that REE represents rare-Earth elements, □ represents vacancy, X represents a mineral that has been reported, and ? represents a questionable report.

Mineral	Formula	Cr			Carmel[1]	Syn[2]	Syn[3]
Included in		11 Crn	11 –	31 –	Crn	Crn	Crn
Anorthite	$CaAl_2Si_2O_8$	–	–	–	X	–	X
Dmisteinbergite	$CaAl_2Si_2O_8$	–	–	–	X	–	–
Dmisteinbergite[4]	$(KCa_3)(Al_7Si_9)O_{32}$	type	–	–	–	–	–
Jingsuiite	TiB_2	type	–	–	X	X	X
Zhiqinite	$TiSi_2$	type	–	–	–	–	–
Badengzhuite	TiP	type	–	–	–	–	–
Unnamed[5]	$Ti_{10}(Si,P,□)_7$	type	–	–	–	–	–
Unnamed[5]	$Ti_{11}(Si,P)_{10}$	type	–	–	–	–	–
Osbornite	Ti(N,C)	X	–	X	X	X	X
Khamrabaevite	Ti(C,N)	X	X	X	X	X	X
Titanium	Ti	X	–	type	–	–	–
Zangboite	$FeTiSi_2$	X	–	type	X	X	–
Moissanite	SiC	X	X	X	X	X	X
Carmeltazite	$ZrAl_2Ti_4O_{11}$	X	–	–	X	X	–
Spinel sensu stricto	$MgAl_2O_4$	–	–	–	X	–	X
Deltalumite	$(Al,Mg,□)Al_2O_4$	X	–	–	X	–	–
Tistarite	Ti_2O_3	–	–	–	X	X	X
Unnamed	FeTiSi	–	–	–	X	X	–
Hibonite	$(Ca,Ce)(Al,Ti,Mg)_{12}O_{19}$	–	–	–	X	X	X
Grossite	$CaAl_4O_7$	–	–	–	X	–	–
Fe	Fe	–	X	X	–	X	X
Tazheranite	$(Zr,Ti,Ca)(O,□)_2$	X	–	–	?	X[6]	–
Baddeleyite	ZrO_2	–	–	–	X[7]	–	–
Britholite	$(REE,Ca,Th,U,Pb)_5(SiO_4)_3O$	X	–	–	–	–	–
Fluorbritholite-(Ce)	$(REE,Ca,Th,U,Pb)_5(SiO_4)_3F$	X	–	–	–	–	
Unnamed[8]	Fe_5Si	–	–	–	X	–	?[9]
Gupeiite	Fe_3Si	–	–	X	X	–	?[9]
Xifengite	Fe_5Si_3	–	–	X[10]	X[10]	X	X[10]
Naquite	FeSi	–	–	type	X	X	X
Linzhiite	$FeSi_2$	–	–	type	–	X	–
Luobusaite	$Fe_{0.84}Si_2$	–	–	type	–	X	–
Hapkeite	Fe_2Si	–	–	–	X	–	–
Silicon	Si	–	X	X	–	–	–
Rutile	TiO_2	X	X	X	–	X	X
Qusongite	WC	–	–	type	–	–	–
Qingsongite	Cubic BN	–	–	type	–	–	–
Coesite (stishovite)	SiO_2	–	–	X	–	–	–
Kyanite	Al_2SiO_5	–	–	X	–	–	–
TiO_2 II	TiO_2	–	–	X	–	–	–
Unnamed	Hexagonal BN	–	X	–	–	–	–
Wüstite	FeO	–	X	X	–	–	–

Note that Crn represents corundum. [1] Mount Carmel, Israel (Griffin et al., 2016a, 2019a; 2020; Xiong et al., 2017). [2] Synthetics in abrasives (Litasov et al., 2019a). [3] Miscellaneous synthetics (Schrewelius, 1948; Filonenko and Lavrov, 1958; Polubelova et al., 1968; Liu and Ownby, 1991; Chinelatto et al., 2001; Sun et al., 2020). [4] New mineral not yet approved by the IMA CNMNC (International Mineralogical Association's Commission on New Minerals, Nomenclature and Classification) (Xiong et al., 2020a). [5] New minerals not yet approved by the IMA CNMNC (Xiong et al., 2020b). [6] Reported as baddeleyite but composition corresponds to tazheranite. [7] Reported as baddeleyite but without compositional or X-ray data. [8] This phase is most likely Si-bearing Fe since a discrete phase of composition Fe_5Si has not yet been reported (Weitzer et al., 2008). [9] Fe silicide with Fe / Si ≈ 3–5 was reported by Litasov et al. (2019a, Fig. 6) based on analyses of ferrosilicon alloy (Cichy, 1972). [10] Reported as "Fe_3Si_2" by Filonenko and Lavrov (1958), Polubelova et al. (1968), Robinson et al. (2004), and Xiong et al. (2017), but the phase is most likely xifengite, first described by Yu (1984), since Fe_3Si_2 has not yet been reported (Weitzer et al., 2008). Sources of data for minerals found as inclusions in corundum at Cr-11 are the following: Xiong et al. (2019b, 2020c); Xiong (unpublished data); Xu et al. (2009, 2013, 2018). Sources of data for minerals not found as inclusions in corundum at Cr-11 are Xu et al. (2009) and Zhang et al. (2016). Sources of data for minerals found only at Cr-31 are listed here (Robinson et al., 2004; Bai et al., 2006; Yang et al., 2008; Li et al., 2009, 2012; Shi et al., 2012; Fang et al., 2009, 2013; Yang et al., 2003, 2015; Dobrzhinetskaya et al., 2009, 2014).

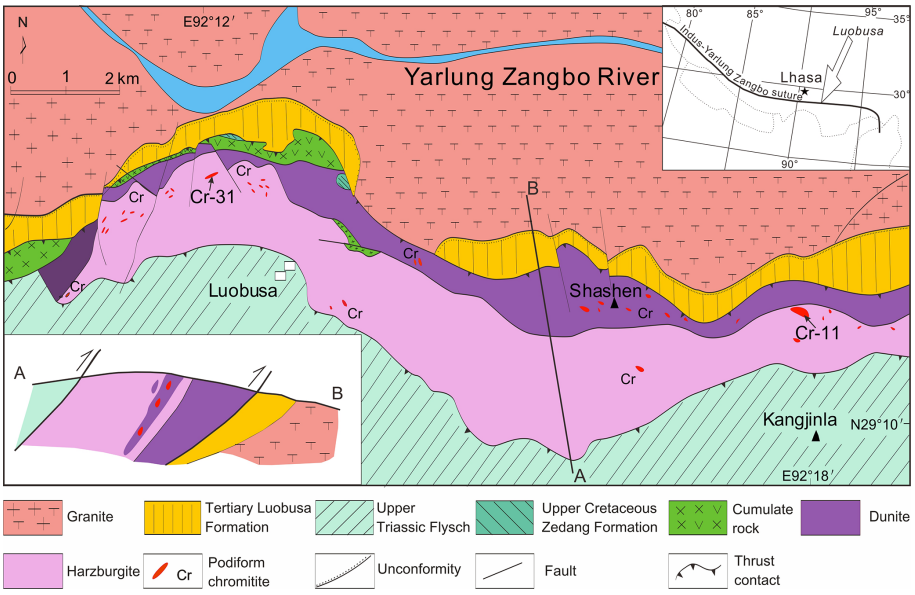

Figure 1. Map and cross section of the Luobusa ophiolite, Tibet, showing podiform chromitite orebodies in the vicinity of Luobusa and Kangjinla. The ophiolite has been overturned. Minerals separated from the orebody Cr-11 are the focus of the present study.

width of ∼ 4 km north–south, resulting in an exposed area of ∼ 70 km^2 (Xu et al., 2015). To the south, it is separated from Triassic flysch by a steep reverse fault and to the north it is thrust over the Tertiary Luobusa Formation and granite of the Gangdese arc (Xu et al., 2014). The ophiolite consists mainly of mantle peridotite and dunite with sparse mafic cumulates. At the base is a thin mélange zone containing dismembered volcanic rocks and cherts that crop out north of the cumulates (Yang et al., 2004). The mantle peridotite consists chiefly of harzburgite and clinopyroxene-bearing harzburgite with minor lherzolite and dunite, whereas the cumulate rocks include wehrlite, pyroxenite, dunite, and gabbro (Wang et al., 1987). Transition-zone dunite, about 100–200 m thick, underlies the entire sequence. The pseudostratigraphy of the ophiolite suggests that it is overturned (Malpas et al., 2003; Yamamoto et al., 2007; Xu et al., 2014; Xiong et al., 2015).

The chromitite orebodies in Luobusa are hosted in harzburgite, where they are typically surrounded by dunite envelopes which are transitional to the peridotites (Wang et al., 1983, 1987; Zhou et al., 1996; Su et al., 2019). Individual orebodies are lenticular, planar podiform or irregular and rarely extend more than a few tens of meters. Fifteen mine groups, clustered into three districts, are recognized, largely on the basis of the nature and distribution of the orebodies. The three districts are, from west to east, labeled Luobusa, Xiangkashan, and Kangjinla. Most of the orebodies lie near the top of the mantle section, except for one deposit hosted in the transitional zone dunite (Wang et al., 2010).

Orebody Cr-11, which is the source of corundum, is enveloped in dunite (Fig. S1a) as are most chromitites in the Luobusa ophiolite. Two major types of podiform chromitite are recognized in the Luobusa ophiolite: massive and disseminated. Massive chromitite typically forms discontinuous layers, 0.5 to 3 m thick, or irregular masses up to 20 m thick. The disseminated chromitites (Fig. S2b, c) have highly varied textures and show strong evidence of formation from magmas in the uppermost mantle. They consist of variable proportions of magnesiochromite and olivine and have banded, nodular, antinodular, and densely disseminated textures.

4 Analytical methods

4.1 Preparation of corundum separates from the Cr-11 chromitite and evidence bearing on a natural versus anthropogenic origin of the corundum

Corundum and the highly reduced minerals included therein were extracted by processing and mineral separation of ∼ 1100 kg of chromitite at the Institute of Multipurpose Utilization of Mineral Resources, Chinese Academy of Geological Sciences, Zhengzhou, including massive, disseminated, and nodular ore from the Cr-11 orebody near Kangjinla. The process was carried out with great care at the institute, as described in detail by Xu et al. (2009, 2015). The samples were first passed through a jaw crusher and then ground in stages to three sizes, and the minerals were separated from each size fraction by a combination of gravity, magnetic, and electrostatic techniques. The mineral concentrates were handpicked under a binocular microscope, and the selected minerals mounted in epoxy and then ground to about half their thickness. The grains were polished using synthetic diamond grinding grease and cleaned in an ultrasonic bath. Xu et al. (2009, 2015) reported that before processing all work

sites and equipment were carefully cleaned to avoid contamination.

Nonetheless, the possibility that the corundum grains extracted from chromitite in the Cr-11 deposit are anthropogenic contamination remains very real since it is very difficult to avoid contamination in separating such minute quantities of material from large amounts of rock (e.g., Evans et al., 2003). Moreover, contamination with anthropogenic alumina poses an even greater threat since alumina has such wide applications in ceramics and abrasives (e.g., Schrewelius, 1948; Filonenko and Lavrov, 1958; Polubelova et al., 1968; Coes, 1971; Cichy, 1972; Chinelatto et al., 2001; Mohammad Sharifi et al., 2010). It is thus not surprising that the case for anthropogenic contamination of the separates from the Luobusa ophiolite has been raised anew and far more forcibly by Litasov et al. (2019a). Citing similarity in mineralogy and textures to those in fused alumina abrasive, as described in the literature, most comprehensively by Filonenko and Lavrov (1958), Polubelova et al. (1968), and in their own paper, Litasov and his colleagues allege that the corundum grains from Cr-11 are none other than brown fused alumina abrasive that was inadvertently introduced into the separate despite the great care taken in processing. A similar rationale led Litasov (2019a) to conclude that a significant proportion of the corundum at Mount Carmel, Israel, could also be fused alumina abrasive, which is a conclusion rebutted by Griffin et al. (2019b) and subsequently defended by Litasov et al. (2019b).

In view of the seriousness of the assertions made by Litasov et al. (2019a), we summarize the arguments, including those made by Litasov et al. (2019a), but not limited to them, for an anthropogenic origin versus a natural origin for the corundum and included phases (Table 1). Arguments for an anthropogenic origin are as follows:

1. The suite of super-reduced minerals reported as inclusions in corundum from Kangjinla is very similar to super-reduced phases in fused alumina, whereas the suite of super-reduced phases from Cr-31, which are not included in corundum, differ significantly (Table 1). The included phases in Cr-11 are distinguished by a more prominent role for Ti than Fe, e.g., carmeltazite, tistarite, osbornite, khamrabaevite, jingsuiite, badengzhuite, and zhiqinite. Few of these minerals are reported from the Cr-31 deposit, which is the type locality for several Fe silicides. A greater role for Fe than Ti would be expected in most rocks.

2. Macroscopically, some corundum grains from Cr-11 are vitreous with a conchoidal fracture (Fig. S2a) similar in appearance to the blue grains of fused alumina illustrated in Litasov et al. (2019a, Fig. 1). Microscopically, the similarity in overall appearance is more striking. In top-polished sections, corundum from Cr-11 and fused alumina are characterized by pockets filled by several super-reduced phases and spheroids of these phases, which are features interpreted to be crystallized alloy melts.

   The minerals included in corundum at Cr-11 have all been synthesized at atmospheric pressure, and there is no indication that pressures greater than 1 bar are required for their stabilization (no data are available on $Ti_{11}(Si,P)_{10}$, $Ti_{10}(Si,P,\square)_7$, or $(KCa_3)(Al_7Si_9)O_{32}$ as none of these minerals have been synthesized). Strictly speaking, exact analogues of the chemically complex tazheranite and britholite have not been synthesized, but simpler isostructural analogues have been, e.g., cubic zirconia (Stubicon and Hellmann, 1981; Fisher, 1986) and britholite (e.g., Fahey et al., 1985; Utsunomiya et al., 2003). Moreover, none of the included minerals are associated with phases requiring high pressure as is the case at Cr-31, where qingsongite and osbornite are associated with coesite pseudomorphs after stishovite, TiO_2-II, and kyanite (Table 1).

3. The presence of corundum in situ in chromitite (Fig. S2b) and in peridotite from near the Cr-11 orebody (Robinson et al., 2015, Fig. 7e, f) has been cited as evidence that corundum in the separates is not a contaminant. Other evidence cited in support of this argument includes discoveries of moissanite in situ in Cr-spinel hosted by dunite in the Kangjinla area (Liang et al., 2015, Fig. 2) and of moissanite and khamrabaevite (TiC) in situ in olivine from the Cr-11 chromitite orebody (Zhang et al., 2016, Fig. 3). However, the in situ corundum grains do not resemble corundum in the separates (e.g., Fig. S2), and it could have a different origin. For example, corundum enclosed in peridotite looks embayed and could be breaking down, whereas its association as grains only 3 µm across with eskolaite (Fig. S2b) suggests that corundum also formed from the local breakdown of chromite. Moissanite is very rare as an inclusion in corundum. The single khamrabaevite (TiC) grain is found among what appear to be fragments of olivine (Zhang et al., 2016, Fig. 3d) and thus can be interpreted as an extraneous particle that became lodged in the mounting medium of the thin section when the nearby olivine broke up during polishing. In summary, it can be argued that the examples so far reported of in situ corundum from the Cr-11 orebody are not sufficiently definitive to refute the hypothesis of an anthropogenic origin for the corundum and the phases included in it.

In defending their contention that the Mount Carmel inclusions are natural, Griffin et al. (2019b) argued that "[the idea that] because something can be made in a laboratory or a factory it cannot occur in nature is to turn the experimental petrology paradigm (i.e., carrying out experiments to understand nature) on its head", which are, in our case, uncontrolled experiments whose objective is to manufacture a product (fused alumina abrasive) as efficiently and cheaply

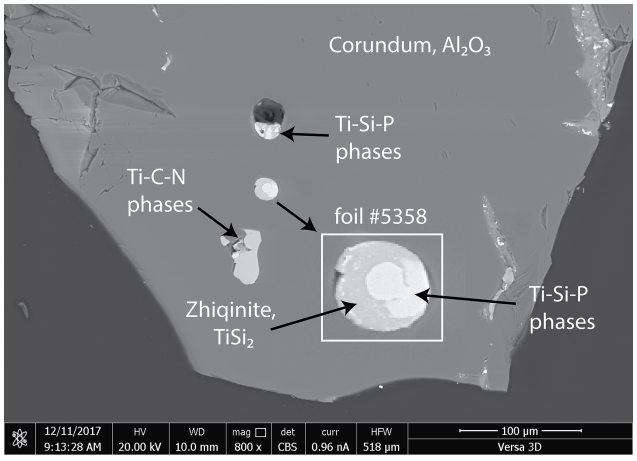

Figure 2. Back-scattered electron (BSE) image of corundum grain enclosing a spheroid composed of Ti–Si–P phases from which foil no. 5358 was taken. Inset shows enlargement of the spheroid in which a mixture of $Ti_{10}(Si,P,\square)_7$ and $Ti_{11}(Si,P)_{10}$ is white and zhiqinite is gray. BSE image taken at the Center for Advanced Research on the Mantle.

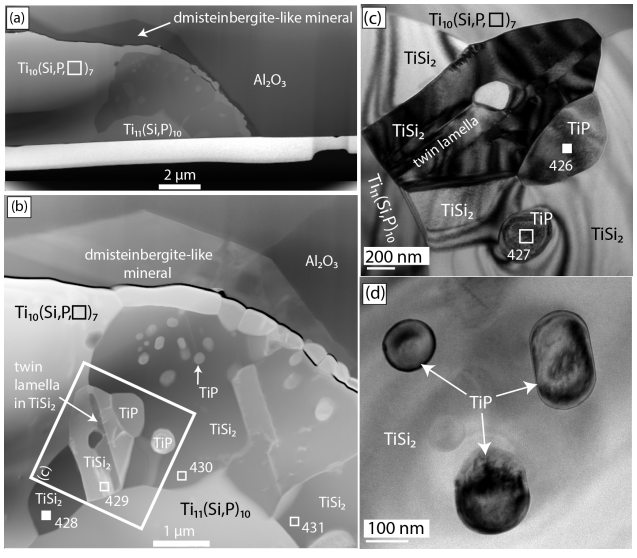

Figure 3. (a) High-angle annular dark-field scanning transmission electron microscope (HAADF-STEM) image of foil no. 5358 showing an aggregate of zhiqinite ($TiSi_2$), enclosing globules of badengzhuite (TiP) and surrounded by $Ti_{10}(Si,P,\square)_7$, $Ti_{11}(Si,P)_{10}$, and the dmisteinbergite-like mineral. **(b)** Al_2O_3 – corundum hosting the Ti silicide inclusion. Source areas for EDX analyses are numbered squares; filled squares indicate locations where data for the structure were obtained: no. 426 (badengzhuite) and no. 428 (zhiqinite). **(c)** TEM (transmission electron microscopy) bright-field image of the area inside the large square shown in **(b)**. **(d)** TEM bright-field image of globular badengzhuite in zhiqinite. HAADF and bright-field images obtained at the GFZ German Research Centre for Geosciences.

as possible. Griffin et al. (2019b) criticized the approach adopted by Lisatov et al. (2019a) as being a "simple comparative approach" that was not "productive". Thus, we will take a closer look at the arguments supporting a natural origin.

1. The presence of corundum, moissanite, and khamrabaevite in situ is more compelling as evidence for the natural origin of these minerals in the separates at Cr-11 than the issues casting doubt on the usefulness of this evidence, which are discussed in argument (3) above.

2. Zhang et al. (2016) reported hexagonal BN as an inclusion in a chromite crystal, from which it can be inferred that boron had been incorporated in the chromitite, most likely from mixing with crustal material. Thus, B could also have been available for incorporation into the alloy melts from which it was precipitated as TiB_2 (jingsuite).

3. Despite the overall similarity in the minerals from Cr-11 and the phases in fused alumina, there are significant differences in detail: zhiqinite ($TiSi_2$), badengzhuite (TiP), and two unnamed minerals, $Ti_{10}(Si,P,\square)_7$ and $Ti_{11}[Si,P]_{10}$ (Xiong et al., 2020b), have not been found in fused alumina despite the availability of the essential constituents Ti, Si, and P in the fused alumina (Litasov et al., 2019a). Conversely, TiP has been reported in an assemblage dominated by Fe silicides in a fulgurite, i.e., an incontrovertibly natural assemblage (Essene and Fisher, 1986). The novelty of the four Ti–Si–P minerals suggests formation under distinctive conditions not attained during the manufacture of fused alumina abrasive.

4. A potassic analogue of dmisteinbergite, $(KCa_3)(Al_7Si_9)O_{32}$ (Xiong et al., 2020a), and deltalumite (see next paragraph) could also be indicative of distinctive conditions during cooling. Litasov et al. (2019a) did not report dmisteinbergite in fused alumina. Filonenko and Lavrov (1958) and Polubelova et al. (1968) reported anorthite, some showing polysynthetic twinning, but made no mention of the two other polymorphs of $CaAl_2Si_2O_8$, which had been synthesized before 1968 (Davis and Tuttle, 1952; Takéuchi and Donnay, 1959), prior to the discovery of a naturally occurring hexagonal polymorph as the mineral dmisteinbergite in 1990. Dmisteinbergite has also been reported from Mount Carmel (Griffin et al., 2018, 2020). The potassic analogue of dmisteinbergite is inferred to have crystallized during rapid cooling as a metastable phase from a silicate melt instead of feldspar (Xiong et al., 2020a), because, if like dmisteinbergite, it is structurally less complex than feldspar (Krivovichev et al., 2012; Zolotarev et al., 2019). Formation of dmisteinbergite and its K analogue have yet to be reported

to form under the conditions of rapid cooling involved in the manufacture of fused alumina abrasive, although fine-grained fused alumina (grain size 300–500 µm comparable to our grains, Fig. S2a) results from rapid cooling (Coes 1971, p. 51; "chill cast", Cichy 1972, p. 2).

5. Deltalumite, $(Al,Mg,\square)Al_2O_4$, the Al-dominant analogue of spinel sensu stricto, $MgAl_2O_4$, is associated with the potassic analogue of dmisteinbergite in foil no. 6034. Griffin et al. (2020) also report a Mg–Al spinel phase from Mount Carmel, which could be deltalumite, in one case associated with dmisteinbergite. Aluminium-dominant spinel has not been reported in fused alumina abrasive, although spinel sensu stricto (identification based on refractive index = 1.733) was reported by Filonenko and Lavrov (1958) and subsequently by Polubelova et al. (1968); Schrewelius (1948) also reported spinel but did not specify its composition. In contrast to type deltalumite, which is tetragonal (Pekov et al., 2019), deltalumite in foil no. 6034 is fully disordered ($a = 7.98(7)$ Å, space group $Fd\bar{3}m$, Enrico Mugnaioli, unpublished structure refinement). This suggests a quench process sufficiently rapid to "freeze in" a high degree of disorder. Like the K analogue of dmisteinbergite, deltalumite formed under physicochemical conditions not attained in the manufacture of fused alumina abrasive, where the only representative of Mg–Al-dominant spinels reported to date is spinel sensu stricto.

In summary, we conclude that the differences between the suite of super-reduced minerals in the separates from the Cr-11 chromitite and the suite of super-reduced phases in fused alumina are more convincing evidence for these minerals having a natural origin than the similarities between them are evidence for an anthropogenic origin. That is, the separates originated in the chromitite, which is an inference backed by the in situ occurrence of corundum, moissanite, and khamrabaevite in chromitite and peridotite. Similarities with the suite reported from Mount Carmel, interpreted to be natural (most recently by Griffin et al., 2019b), provide further support of a natural origin for the Cr-11 minerals.

Nonetheless, there remain opportunities for further study of the phases included in corundum to see whether there are constraints on formation conditions that could provide more conclusive arguments. For example, the Fe–Si–Ti system could provide such constraints (Weitzer et al., 2008; Ross et al., 2019). In the subsystem Fe–Si, the stable phases at atmospheric pressure are Fe_3Si (gupeiite) and Fe_5Si_3 (xifengite). Gupeiite has been reported from Mount Carmel, whereas suessite (Fe_3Si) has not been reported as an inclusion in corundum at either Mount Carmel (Cr-11 or Cr-31) or in abrasives. Hapkeite (Fe_2Si) occurs in distinctive environments, including the lunar regolith and ureilite meteorites (Ross et al., 2019), as well as at Mount Carmel.

Table 2. Energy-dispersive spectroscopic (EDX) analyses of badengzhuite in foil no. 5358.

Analysis no.	426	427	Average	SD
	Net uncorrected counts			
C	0	0		
O	35	27		
Si	105	310		
P	1070	1014		
Ti	1486	1545		
	Weight percent, wt % (1σ)			
P	39.44 (1.74)	37.26 (1.67)	38.35	1.54
Ti	60.56 (2.50)	62.74 (2.56)	61.65	1.54
	Atomic percent, at. %			
P	50.17	47.86	49.02	1.63
Ti	49.83	52.14	50.99	1.63
Sum	100	100	100	

4.2 Transmission electron microscopy and focused ion beam methodology

At the GFZ Potsdam, transmission electron microscopy (TEM) and focused ion beam (FIB) were used to determine the composition of the minerals included in corundum (for details about the method, see Wirth, 2004, 2009). TEM requires that samples are prepared as foils sufficiently thin to be transparent to electrons (generally, the foil thickness is less than 200 nm). Electron-transparent foils were prepared with a FIB. Typical TEM foils have dimensions of 15 µm × 10 µm × 0.20 µm. A FIB single-beam device (FEI FIB 200 TEM) was used for sample preparation. For this, a Ga ion beam (30 keV acceleration voltage) was focused onto a selected location of the sample surface to sputter material from the sample. In order to facilitate the sputtering process, water vapor is used together with the Ga ions.

4.3 Simulated powder X-ray diffraction patterns

Simulated powder X-ray diffraction patterns were obtained with Powder Cell. Radiation was Cu Kα and angular limit was 90° (about 1.0 Å).

4.4 Energy dispersive and three-dimensional electron diffraction analyses

Energy dispersive X-ray spectroscopy (EDX) and 3D electron diffraction (3D ED) analyses (Gemmi et al., 2019) were carried out on a Zeiss Libra 120 TEM operating at 120 kV and equipped with a LaB_6 source and a Bruker EDX XFlash6T-60 detector, at the Center for Nanotechnology Innovation@NEST, one of the centers of the Istituto Italiano di Tecnologia located in Pisa, Italy.

Table 3. Energy-dispersive spectroscopic (EDX) analyses of zhiqinite in foil no. 5358.

Analysis no.	428	429	430	431	Average	Standard deviation
	Net uncorrected counts					
C	50	37	29	19		
O	36	43	47	8		
Si	1842	1784	2154	2788		
Ti	1187	1273	1241	1839		
	Weight percent, wt % (1σ)					
Si	57.69 (1.40)	55.21 (1.36)	60.42 (1.35)	57.13 (1.31)	57.61	2.15
Ti	42.31 (1.85)	44.79 (1.92)	39.58 (1.71)	42.87 (1.70)	42.39	2.15
	Atomic percent, at. %					
Si	69.92	67.75	72.24	69.44	69.84	1.85
Ti	30.08	32.25	27.76	30.56	30.16	1.85
Sum	100	100	100	100	100	

For EDX analysis, we did not use specific standards and thus the weight percents reported in Tables 2 and 3 derive from the initial calibration of the instrument. Our EDX method used the thin-specimen approximation by Cliff and Lorimer (1975).

3D ED was performed in STEM mode after defocusing the beam in order to have a parallel Köhler illumination on the sample. A beam size of about 150 nm in diameter was obtained by inserting a 5 µm C2 condenser aperture. An extremely low dose of illumination was used in order to avoid any possible amorphization of the sample.

Data collection was performed in angular steps of 1° with total tilt ranges of 73 and 80° for badengzhuite and zhiqinite, respectively. The useful tilt range was limited by the thickness of the FIB lamella. After each tilt, a diffraction pattern was acquired and crystal position tracked by defocused STEM imaging. During the experiment, the beam was precessed around the optical axis by an angle of 1° (Vincent and Midgley, 1994), as first described by Mugnaioli et al. (2009). Precession was obtained using a Nanomegas Digistar P1000 device. Diffraction patterns were recorded by an ASI Timepix single-electron camera (Nederlof et al., 2013; Gemmi and Lanza, 2019). A camera length of 180 mm was used, equivalent to a theoretical resolution of 0.8 Å.

3D ED data were analyzed using the software PETS (Palatinus et al., 2019). The ab initio structure determination was obtained by Standard Direct Methods (SDM) as implemented in the software SIR2014 (Burla et al., 2015). For structure determination, data were treated with a fully kinematical approximation, i.e., neglecting dynamical scattering and assuming that I_{hkl} was proportional to $|F_{hkl}|^2$.

Least-squares structure refinement was performed with the software JANA2006 (Petříček et al., 2014) using the dynamical refinement procedure described by Palatinus et al. (2015). Only 55 out of 74 and 65 out of 81 diffraction patterns, mostly belonging to the central part of the data sets, were actually used for the refinement of badengzhuite and zhiqinite, respectively. Patterns obtained at high tilt angles were unsuitable for study because of the high absorption resulting from the increased thickness of the FIB lamella. During the refinement process, the thickness of the lamella at 0° tilt was estimated to be about 30–50 nm. Final residuals $R(3\sigma)$ were 0.0951 for badengzhuite and 0.1015 for zhiqinite. All structure information for both minerals is available as CIF files in the Supplement.

The visualization of the 3D ED data was obtained by the software ADT3D (Kolb et al., 2011), and images of the structure were made with the software VESTA (Momma and Izumi, 2011).

5 Results

5.1 Occurrence of badengzhuite and zhiqinite

The corundum enclosing badengzhuite, zhiqinite, and other highly reduced phases occurs as translucent to transparent grains generally exceeding 200 µm and having a vitreous luster; many grains are pink in color; others are colorless, light yellow, and light brown (Fig. S2a, Xu et al., 2013, Fig. 2). Badengzhuite and zhiqinite were found in a single spheroid 20 µm in diameter composed in roughly equal proportions of zhiqinite and a mixture of the potentially new minerals $Ti_{10}(Si,P,\square)_7$ and $Ti_{11}(Si, P)_{10}$ (foil no. 5358, Figs. 2 and 3). The spheroid is partly surrounded by a halo of a dmisteinbergite-like mineral, $KCa_3(Al_7Si_9)O_{32}$, which is also potentially new. Badengzhuite occurs as globules up to about 0.5 µm across and an oval grain nearly 1 µm long enclosed in an aggregate of zhiqinite. No direct contacts of badengzhuite with the dmisteinbergite-like mineral were ob-

served, but one to two badengzhuite globules appear to contact the Ti–Si–P phases. Zhiqinite grains are mostly 1 to 2 µm long and are mostly tabular. A possible second occurrence of zhiqinite, for which an EDX analysis gave a Si / Ti ratio of ∼2, constitutes the entirety of an inclusion 25 µm × 30 µm across in another corundum grain.

5.2 Physical properties and morphology of badengzhuite and zhiqinite

The grains of badengzhuite and zhiqinite are too small to determine their physical properties. Both minerals are presumably opaque. Synthetic TiP is gray to black, brittle, and has a metallic luster (Gewecke, 1908; Biltz et al., 1938; Knausenberger et al., 1965); its measured density is 3.95 g cm^{-3} according to Gewecke (1908) and 4.08 g cm^{-3} according to Ripley (1962). The density calculated from the ab initio structure solution is 4.233 g cm^{-3}.

Synthetic $TiSi_2$ is white to gray in color and has a metallic luster (Laves and Wallbaum, 1939; Cotter et al., 1956). Its Mohs hardness is 4–5 (Hönigschmid, 1906) and its Vickers hardness number (VHN) load 1 kPa (HV1) hardness is 870 ± 15 kg mm^{-2} (Frommeyer and Rosenkranz, 2004). The density measured on synthetic $TiSi_2$ is 4.07 g cm^{-3} (Frommeyer and Rosenkranz, 2004). The density calculated from the ab initio structure solution is 4.136 g cm^{-3}.

No forms or twinning were observed in badengzhuite, although twinning is frequently encountered in the synthetic analogue (Snell, 1967).

No forms were observed for zhiqinite, but the tabular habit could result from flattening parallel to (110). The synthetic analogue forms crystals between 0.6 and 7 mm long having a platy, acicular, or polyhedral habit (Hönigschmid, 1906; Peshov and Kristov, 1986; Laves and Wallbaum, 1939). Laves and Wallbaum (1939) described crystals of the synthetic analogue as bipyramidal with orthorhombic (pseudotetragonal) symmetry and reported that faces of the form {111} gave an a : b : c ratio in good agreement with the a : b : c ratio calculated from their powder X-ray data.

5.3 Chemical compositions of badengzhuite and zhiqinite

Badengzhuite and zhiqinite were analyzed by EDX (Tables 2 and 3). Grains are too fine and sparse for analyzing H_2O or CO_2 by traditional methods. However, only a few net counts of O were detected during EDX analyses, and we conclude that O is not present and, by extension, neither is H_2O nor CO_2.

EDX scans of badengzhuite showed major P, Ti, and Cu (e.g., Fig. S3 in the Supplement); the last element can be attributed to the focused ion beam foil support grid, specifically from the prong to which the foil is attached. Significant Si was detected; this we attribute to contamination from the surrounding $TiSi_2$ (zhiqinite) as the analyzed badengzhuite grains are so small (≤ 1µm, Fig. 3). The empirical formula of badengzhuite calculated on the basis of two cations is $Ti_{1.020}P_{0.980}$. The simplified formula is TiP, as is the ideal formula, which requires 60.71 wt % Ti and 39.29 wt % P; the total is 100 wt %.

EDX scans of zhiqinite only showed major Si, Ti, and Cu (e.g., Fig. S4 in the Supplement); the last element can again be attributed to the focused ion beam foil support grid. The empirical formula of zhiqinite calculated on the basis of three cations is $Ti_{0.905}Si_{2.095}$. The simplified formula is $TiSi_2$, as is the ideal formula, which requires 46.01 wt % Ti and 53.99 wt % Si; the total is 100 wt %.

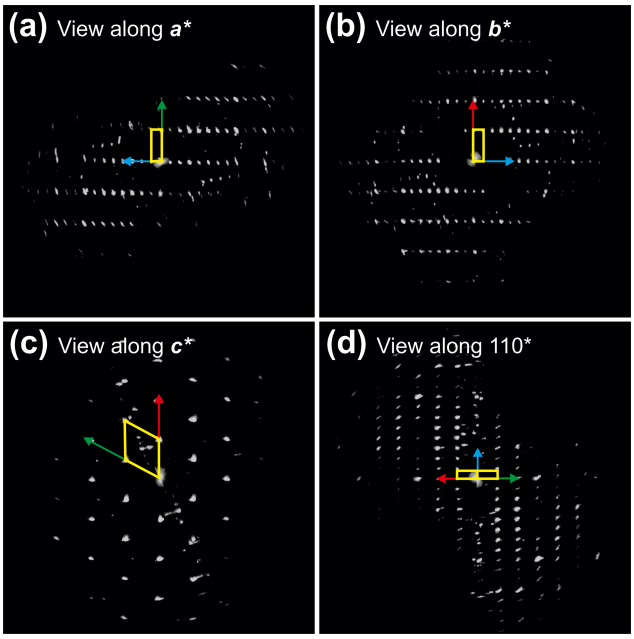

Figure 4. 3D reconstruction of electron diffraction data taken from badengzhuite (TiP) at point no. 426 (Fig. 3c). **(a)** View along 100*. Reflections belonging to a second crystalline individual, probably the hosting zhiqinite ($TiSi_2$) domain, were occasionally sampled and therefore appear in the 3D reconstruction. **(b)** View along 010*. **(c)** View along 001*. **(d)** View along 110*. Extinction rule $hh\overline{2}hl : l = 2n$ is not evident in projection due to the occurrence of extra reflections not belonging to the badengzhuite (TiP) domain. Cell edges are sketched in yellow. Red arrow indicates a^* direction, green arrow indicates b^* direction and blue vector indicates c^* direction.

5.4 Crystallography of badengzhuite and zhiqinite

Because of the very limited amount of material available, it was not possible to collect X-ray powder diffraction data for powder patterns.

Single-crystal diffraction data of badengzhuite and zhiqinite were therefore obtained by three-dimensional electron diffraction (3D ED) from several submicrometric crystals spotted in foil no. 5358. Badengzhuite data were taken at

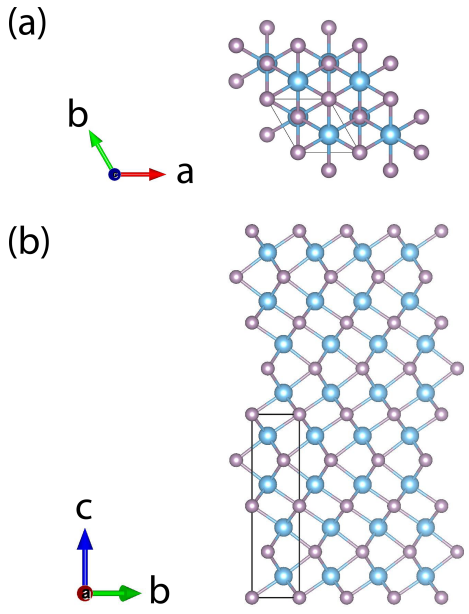

Figure 5. Crystal structure of badengzhuite. **(a)** View along c; **(b)** view along b.

Table 4. Atomic coordinates for badengzhuite.

Label	x/a	y/b	z/c	U_{iso}	Multiplicity	Occupancy
Ti1	1/3	2/3	0.1170(3)	0.0055(11)	4	1
P1	0	0	0	0.0076(15)	2	1
P2	2/3	1/3	1/4	0.0124(17)	2	1

point 426 (Fig. 3c) and gave an hexagonal lattice with extinctions and symmetry consistent with space group $P6_3/mmc$ (no. 194). Cell parameters are $a = 3.49(7)$ Å, $c = 11.7(2)$ Å, $V = 124(4)$ Å^3, and $Z = 4$. Reconstructed 3D ED data of badengzhuite are shown in Fig. 4 and the atomic coordinates given in Table 4. The structure (Fig. 5) is essentially identical with that of synthetic TiP (Snell, 1967). Ti atoms are octahedrally coordinated with six P atoms. Ti–P1 interatomic distance is 2.44(5–10) and Ti–P2 distance is 2.55(5–10) Å. The basic building block of the badengzhuite structure consists of a couple of face-sharing Ti octahedra. These blocs are reciprocally connected by edge sharing, forming along c a kinked stacking of hexagonal close-packed layers.

Single-crystal studies of zhiqinite were carried out by 3D ED at several points of foil no. 5358. The data set used for the final structure refinement came from point 428 (Fig. 3b). Zhiqinite has orthorhombic symmetry and space group $Fddd$ (no. 70). Unit cell parameters are $a = 8.18(16)$ Å, $b = 4.85(10)$ Å, $c = 8.42(17)$ Å, $V = 334(12)$ Å^3, and $Z = 8$. Reconstructed 3D ED data of zhiqinite are shown in Fig. 6 and the atomic coordinates given in Table 5. The structure (Fig. 7) is essentially identical with that of synthetic $TiSi_2$ (form C54) (Jeitschko, 1977; Li et al., 2013). Ti atoms are

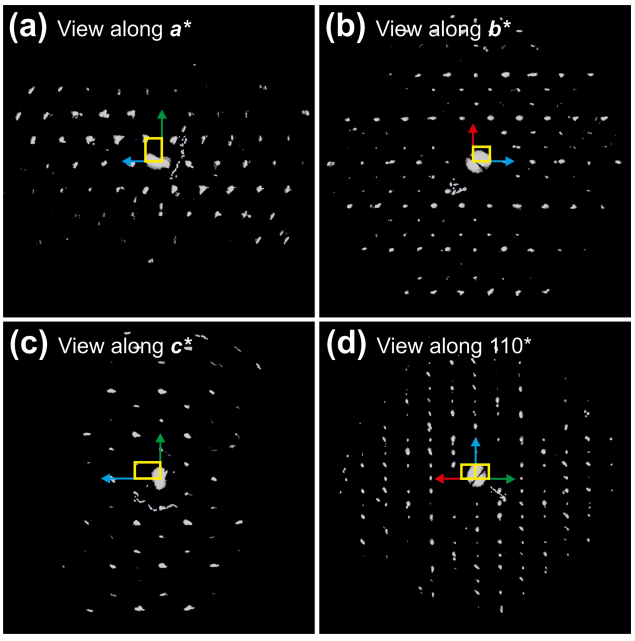

Figure 6. 3D reconstruction of electron diffraction data taken from zhiqinite ($TiSi_2$) at point no. 428 in foil no. 5358 (Fig. 3b). **(a)** View along 100*. Chess-board extinctions due to the F-centered lattice are evident. **(b)** View along 010*. **(c)** View along 001*. **(d)** View along 110*. Reflections $hk0$ are present only for $h + k = 4n$ due to the occurrence of the d-glide plane (001). Cell edges are sketched in yellow. Red arrow indicates a^* direction, green arrow indicates b^* direction and blue vector indicates c^* direction.

Table 5. Atomic coordinates for zhiqinite.

Label	x/a	y/b	z/c	U_{iso}	Multiplicity	Occupancy
Ti1	0.125	0.125	0.125	−0.0032(16)	8	1
Si1	0.4528(14)	0.125	0.125	0.0028(20)	16	1

coordinated with 10 Si atoms. Ti–Si interatomic distances range from 2.51(8) to 2.80(5) Å.

Contrast change in Fig. 3 revealed the presence of several lamellae inside zhiqinite domains. 3D ED, performed at point 429, revealed that this contrast is related to a twin lamella related to the host by rotation in the (110) plane around c^*, which exchanges (110) and (1–10) (Fig. 8).

Cotter et al. (1956) reported a second polymorph of $TiSi_2$, the C49 form, which is a layered structure less dense than C54 (calculated density $= 3.85\,g\,cm^{-3}$) in which Ti is coordinated with only eight Si. We saw no evidence that the twinning in zhiqinite is related to transition from C49 to C54.

Simulated powder X-ray diffraction patterns are given in Tables S1 and S2 and in Figs. S5 and S6 in the Supplement for badengzhuite and zhiqinite, respectively. They were calculated using the structure obtained by 3D ED.

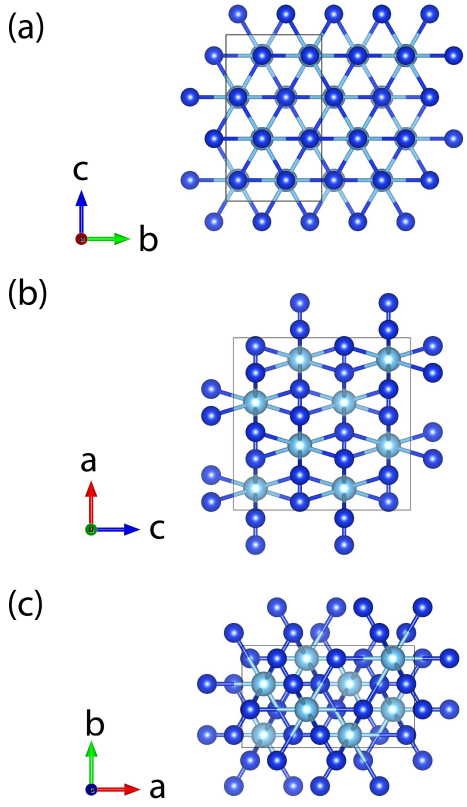

Figure 7. Crystal structure of zhiqinite. **(a)** View along a; **(b)** view along b; **(c)** view along c.

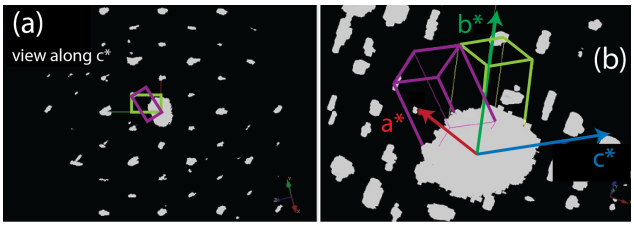

Figure 8. 3D reconstruction of electron diffraction data taken from twins in zhiqinite near point no. 429 in foil no. 5358 (Fig. 3). **(a)** View along c^*, which is the axis of rotation for the twins (green and purple rectangles). **(b)** Tilted view showing c^*, which is common to both twins, as well as a^* and b^* in the twin outlined in yellow green.

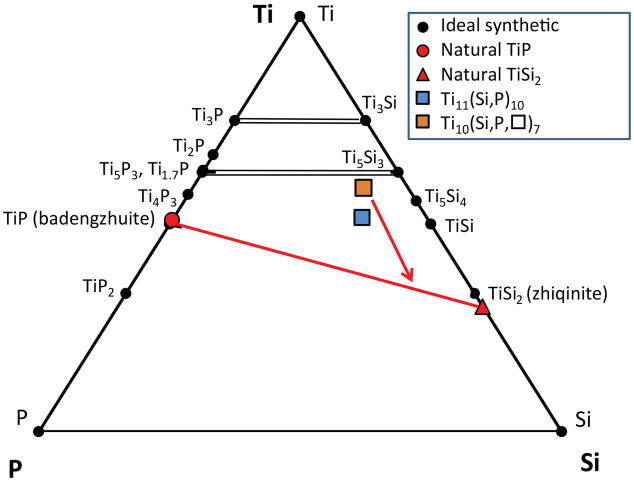

Figure 9. Plot of compounds in the ternary Ti–Si–P system in foil no. 5358. Data on the natural phases are averages of two to four EDX analyses. Source of data: badengzhuite and zhiqinite (Tables 2 and 3); $Ti_{10}(Si,P,\square)_7$ and $Ti_{11}(Si,P)_{10}$ (F. Xiong et al., unpublished data). Synthetic Ti–P phases are from Okamoto (2007); synthetic Ti–Si phases are from Fiore et al. (2016). Dashed brown lines: possible solid solution between isostructural Si and P phases. Solid red line: tie line for foil no. 5358. Red arrow shows inferred crystallization sequence for the ternary melt yielding the spheroid in foil no. 5358.

6 Discussion

6.1 Melting in the ternary Ti–Si–P system.

Badengzhuite, zhiqinite, $Ti_{11}(Si,P)_{10}$, and $Ti_{10}(Si,P,\square)_7$ in foil no. 5358 are composed almost exclusively of Ti, Si, and P (Fig. 9), with a maximum of 2 wt % V, 3 wt % Cr, 2 wt % Mn, and 2 wt % Fe in the latter two phases (Xiong et al., unpublished data). The latter two phases are the first ternary Ti–Si–P solid solutions to be reported either in minerals or in synthetics. Several binary Ti–P and Ti–Si phases have been synthesized (Okamoto, 2007; Fiore et al., 2016), but only two compositions have isostructural analogues in both the Ti–Si and Ti–P systems: Ti_3Si and Ti_3P (Ti_3P type; Lundström, 1969) and $Ti_{10}Si_6$ and $Ti_{10}P_6$ (Mn_5Si_3 type, Nowotny, 1963, Lundström, 1969). The ternary compound $Ti_{10}(Si,P,\square)_7$ is also isostructural with Mn_5Si_3 (Xiong et al., 2020b).

Inspection of the bounding Ti–P and Ti–Si binary systems (Fig. 10) reveals a possible crystallization path (Fig. 9). Because phases isostructural with Ti_5P_3 and Ti_5Si_3 melt to liquids of the same composition at the highest temperatures in their respective binary systems, $Ti_{10}(Si,P,\square)_7$ would be expected to crystallize first in the ternary system. Crystallization is inferred to have proceeded with the intermetallic melt becoming less titanian. In the binary systems, successive phases crystallize peritectically, including TiP and $TiSi_2$. However, the binary phases Ti_4P_3, Ti_5Si_4, and TiSi were not found in the spheroid; instead, we have the ternary phase $Ti_{11}(Si,P)_{10}$, which does not correspond to any of the binary phases shown in Fig. 10 (Xiong et al., 2020b). Crystallization of the melt appears to have concluded with the formation of the assemblage badengzhuite-zhiqinite, both of which are binary phases. In summary, $Ti_{10}(Si,P,\square)_7 \rightarrow Ti_{11}(Si,P)_{10} \rightarrow TiSi_2 + TiP$.

The temperature ranges relevant to $Ti_{10}(Si,P,\square)_7$, $TiSi_2$, and TiP (Fig. 10) are 2100–1600 °C for the Ti–P binary (Ohtani et al., 2006) and 2130–1330 °C for the Ti–Si bi-

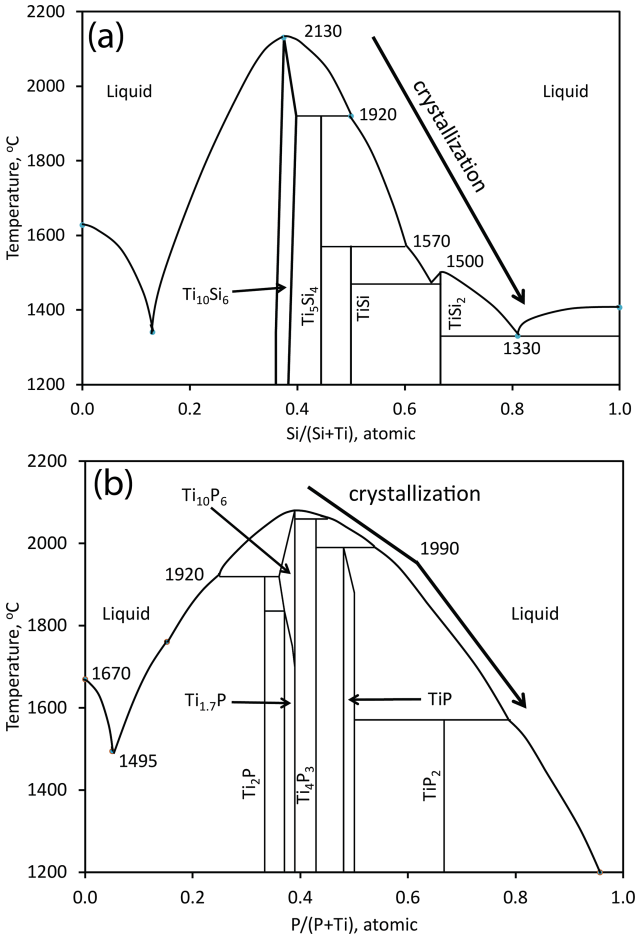

Figure 10. (a) The Ti–Si binary (modified from Fiore et al., 2016, Fig. 2a) **(b)** The Ti–P binary (modified from Ohtani et al., 2006, Fig. 5a; Okamoto, 2007, Fig. 1). The arrows show the inferred crystallization sequence in the two binary systems corresponding to the crystallization sequence in the ternary system (Fig. 9).

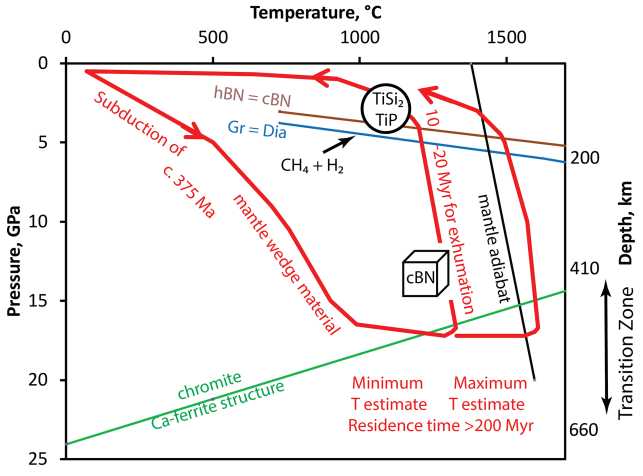

Figure 11. Pressure–temperature diagram summarizing evolution of the Luobusa ophiolite as it relates to badengzhuite, zhiqinite, and associated phases in foil no. 5358 (modified from Griffin et al., 2016b, Fig. 11) with P–T estimate for qingsongite (cubic BN) from Dobrzhinetskaya et al. (2014), graphite–diamond transition (Gr-Dia) from Day (2012), and hexagonal BN-qingsongite (hBN-cBN) from Corrigan and Bundy (1975). Interaction with highly reducing $CH_4 + H_2$ fluids occurred during exhumation.

nary (Svechnikov et al., 1970; Fiore et al., 2016). However, the temperature range for the the ternary system could be much lower; for example, temperatures of an eutectic between TiP and $TiSi_2$ could be well below the temperatures for the Ti_4P_3–TiP peritectic at 1990 °C in the Ti–P binary and for the TiSi–$TiSi_2$ eutectic at 1470 °C or the Si–$TiSi_2$ eutectic at 1330 °C in the Ti–Si binary. Moreover, the ternary $Ti_{10}(Si,P,\square)_7$ phase would be expected to have crystallized at a lower temperature than either binary analogue. Comparison with the impact of Fe on the Ti–Si system (Weitzer et al., 2008) suggests that the impact of P on the Ti–Si system could be several hundreds of degrees Celsius and melting of Ti–Si–P mixtures is plausible at temperatures in the upper mantle.

In regards to a minimum temperature of crystallization, we note that in the preparation of $TiSi_2$ nanofilms the C54 polymorph appears to form stably above 700–800 °C, whereas at lower temperatures the metastable C49 polymorph was reported (Beyers and Sinclair, 1985).

6.2 Origin of Ti–Si–P melts

Robinson et al. (2015), Xiong et al. (2015), and Xu et al. (2015) presented what has been the prevailing scenario for the deep-seated origin of highly reduced mineral assemblages of possible crustal origin, together with clearly crustal minerals such as zircon, in Luobusa ophiolitic peridotites and chromitites, where they are associated with UHP minerals including coesite (after stishovite) and other minerals consistent with crystallization at a depth of > 300 km (Yang et al., 2007; Dobrzhinetskaya et al., 2009, 2014). The presence of boron (qingsongite, cubic BN) is further evidence for a crustal origin of the stishovite/coesite-bearing assemblage. Preservation of these minerals in chromitites and peridotites implies effective isolation from the mafic melts that crystallized to form the ophiolites. The chromite grains containing these minerals were believed to have been carried in melt channels to suprasubduction mantle wedges and then deposited as podiform chromitites near the Moho. The subsequent rise of asthenospheric peridotites into suprasubduction zones was facilitated by subduction initiation and possibly by slab tear.

Griffin et al. (2016b) and Xiong et al. (2017) have proposed an alternative scenario for the highly reduced assemblages containing intermetallic phases not associated with ultrahigh-pressure minerals (Table 1; Fig. 11); that is, their model for highly reduced phases at Mount Carmel, Is-

rael, can be applied to the Luobusa ophiolite. This model envisages interaction of mantle-derived $CH_4 + H_2$ fluids with basaltic magmas within a previously subducted mantle wedge during its rapid exhumation from the deep upper mantle to the shallow lithosphere (depths of ∼ 30–100 km). Exhumation resulted in precipitation of corundum. Although analogues of highly reduced intermetallic minerals found in the Cr-11 chromitite were largely synthesized at atmospheric pressure; Li et al. (2013) reported synthesis of $TiSi_2$ at pressures as high as ∼ 52 GPa, implying that these minerals could have formed at pressures up to ∼ 5 GPa as shown in Fig. 11.

Griffin et al. (2020) emphasized the role of melting in the origin of jingsuiite and other intermetallic compounds at Mount Carmel, where they occur in melt pockets trapped in corundum aggregates, which are found as xenoliths in basalt in Cretaceous volcanoes. Textures are cited as evidence of immiscibility between metallic (Fe–Ti–C–Si) melts, Ti–(oxy)nitride melts, and Ca–Al–Mg–Si–O "oxide" melts. The metallic melts commonly form spherules in oxide glass. The parageneses in the melt pockets of the xenoliths require oxygen fugacities more reducing than 6 log units below the oxygen fugacities corresponding to the iron–wüstite buffer; these are conditions they believed were generated by interaction between evolved silicate melts and mantle-derived $CH_4 + H_2$ fluids near the crust–mantle boundary. Estimates of the pressure at Mount Carmel are constrained to be near 1 GPa by (1) the abundance of corundum since experiments in the model $CaO–Al_2O_3–SiO_2$ system indicate that anorthite melts incongruently to give corundum only above 1 GPa (Hariya and Kennedy, 1968; Goldsmith, 1980; Ottonello et al., 2013) and (2) the presence of grossite ($CaAl_4O_7$) in some highly reduced xenoliths, which implies that pressures should not have exceeded 1 GPa (Ottonello et al., 2013). In regards to temperature, Griffin et al. (2020) suggested it decreased from > 1450 to ∼ 1200 °C.

Applying the scenario proposed for Mount Carmel to Luobusa ophiolite raises several questions. As pointed out by Griffin et al. (2020), the Luobusa and Mount Carmel parageneses have many features in common, notably evidence for intermetallic melts and silicate melts in pockets enclosed in corundum. However, in contrast to Mount Carmel, the only evidence for silicate melts in foil no. 5358 is the dmisteinbergite-like mineral (Fig. 3). Compositionally, the dmisteinbergite-like mineral, $KCa_3(Al_7Si_9)O_{32}$, corresponds to a aluminous granodioritic melt (approximately 40 % anorthite, 10 % orthoclase, 5 % $SrAl_2Si_2O_8$, 11 % Al_2SiO_5, and 35 % quartz modified from Xiong et al., 2020a). The dmisteinbergite-like mineral could have resulted from the quenching of this aluminous granodioritic melt consistent with the interpretation suggested for other occurrences of dmisteinbergite, the hexagonal analogue of anorthite, $CaAl_2Si_2O_8$, which crystallized metastably instead of feldspar during rapid cooling from a silicate melt (Krivovichev et al., 2012; Zolotarev et al., 2019). Less obvious is whether the granodioritic melt is from the larger magmatic body from which corundum precipitated. Instead, the halo of granodioritic melt in foil no. 5358 could have formed by exsolution of a much more subordinate immiscible silicate melt from a dominantly Ti–Si–P intermetallic melt and thus have a local origin. In this case, the granodioritic composition of this melt would give no indication of the composition of the presumably basaltic melt from which the corundum precipitated. We can only speculate that this melt was sufficiently close to anorthite in composition and that the minimum pressure can be estimated from the experimental data to be 1 GPa when the melt cooled. Grossite has not yet been found in the Cr-11 chromitite, but the presence of hexagonal BN in chromite (Zhang et al., 2016) implies pressures less than 4–5 GPa (Fig. 11). Temperatures of > 1450 to ca. 1200 °C deduced for Mount Carmel (Griffin et al., 2020) are in the range suggested by phase relationships in the Ti–Si–P system in foil no. 5358. Conditions could have been even more reducing than 6 log units below the iron–wüstite buffer. Ulmer et al. (1998, Fig. 1a, p. 295) showed a Ti–TiO buffer over 10 log units more reducing than iron–wüstite (Litasov et al., 2019a, Fig. 7, showed a difference of ∼ 10 log units). Thus, oxygen fugacities corresponding to the Ti–TiO buffer might best approximate the stability of the Ti phases in the spheroid.

7 Conclusion

Minerals enclosed in corundum separated from the Cr-11 chromitite orebody in the Luobusa ophiolite at Kangjinla, Tibet, include two the new highly reduced minerals badengzhuite (TiP) and zhiqinite ($TiSi_2$), as well as three potentially new minerals: $(KCa_3)(Al_7Si_9)O_{32}$, $Ti_{11}(Si,P)_{10}$, and $Ti_{10}(Si,P,\square)_7$. Together, the four highly reduced Ti minerals constitute a spheroid 20 µm across inferred to have crystallized from a droplet of Ti–Si–P intermetallic melt. We suggest that interaction of mantle-derived $CH_4 + H_2$ fluids with basaltic magmas in the shallow lithosphere (depths of ∼ 30–100 km) under conditions more reducing than 6 log units below the oxygen fugacities corresponding to the iron–wüstite buffer resulted in precipitation of corundum that entrapped intermetallic melts, some of which crystallized to ultra-reduced Ti–P–Si phases. Experimental work on the Ti–Si and Ti–P systems indicates that the Ti minerals enclosed in corundum could have crystallized from the alloy melt at the lowest temperature accessible on the liquidus.

Litasov et al. (2019a, b) have alleged that these super-reduced Ti-rich phases are anthropogenic contaminants inadvertently introduced with fused alumina abrasive during preparation of mineral separates from the chromitite. However, we conclude that the differences between the suite of super-reduced minerals in the separates from chromitite Cr-11 at Kangjinla and the suite reported by Litasov et al. (2019a, b) are convincing evidence for the Kangjinla minerals having a natural origin. Less compelling are the simi-

larities cited by Litasov et al. (2019a, b) as evidence for an anthropogenic origin of the Kangjinla suite.

Code and data availability. All data derived from this research are presented in the enclosed tables and figures, and crystallographic data for badengzhuite and zhiqinite are available in the Supplement.

Supplement. The supplement related to this article is available online at: https://doi.org/10.5194/ejm-32-557-2020-supplement.

Author contributions. FX, XX, and JY undertook the fieldwork, collected the rock samples, and acquired a portion of the analytical data. FX, XX, JY, and PTR conceived the project, studied the microscopic and submicroscopic features, and interpreted the elemental data. EM, MG, and RW carried out TEM and FIB work and determination of the crystal structure. FX and EG wrote the article and finalized the submission. All authors have approved the submitted version.

Competing interests. The authors declare that they have no conflict of interest.

Acknowledgements. Enrico Mugnaioli and Mauro Gemmi acknowledge the Regione Toscana for funding the purchase of the ASI Timepix detector through the FELIX project (Por CREO FESR 2014–2020 action).

We thank the two anonymous reviewers for their constructive comments on an earlier version of the article.

Financial support. This research has been supported by the Second Tibetan Plateau Scientific Expedition and Research Program (no. 2019QZKK0801), the National Key Research and Development Project of China (no. 2016YFC0600310), Key Special Project for Introduced Talents Team of Southern Marine Science and Engineering Guangdong Laboratory (Guangzhou) (no. GML2019ZD0201), the Key Laboratory of Deep-Earth Dynamics of Ministry of Natural Resources Fund (no. J1901-7, J1903), the National Natural Science Foundation of China (NNSFC; nos. 41672046, 41641015, 41720104009, 41703036, 41703053), and the China Geological Survey (CGS; project no. DD201190060).

Review statement. This paper was edited by Sergey Krivovichev and reviewed by two anonymous referees.

References

Bai, W. J., Shi, N. C., Fang, Q. S., Li, G. W., Xiong, M., Yang, J. S., and Rong, H.: Luobusaite – A New Mineral, Act. Geol. Sin., 80, 656–659, https://doi.org/10.1111/j.1755-6724.2006.tb00289.x, 2006.

Beyers, R. and Sinclair, R.: Metastable phase formation in titanium-silicon thin films, J. Appl. Phys., 57, 5240–5245, https://doi.org/10.1063/1.335263, 1985.

Biltz, W., Rink, A., and Wiechmann, F.: Beiträge zur systematischen Verwandtschaftslehre. 83. Über die Verbindungsfähigkeit von Titan mit Phosphor, Z. Anorg. Allg. Chem., 238, 395-405, 1938

Burla, M. C., Caliandro, R., Carrozzini, B., Cascarano, G. L., Cuocci, C., Giacovazzo, C., Mallamo, M., Mazzone, A., and Polidori, G.: Crystal structure determination and refinement via SIR2014, J. Appl. Crystallogr., 48, 306–309, https://doi.org/10.1107/S1600576715001132, 2015.

Chinelatto, A. S. A., Contardi, O. A., Pallone, E. M. J. A., and Tomasi, R.: Production of Alumina Matrix Nanocomposites with Inclusions of TiC and TiB_2, via Reactive Milling, Key Eng. Mater., 189–191, 208–215, https://doi.org/10.4028/www.scientific.net/kem.189-191.208, 2001.

Cichy, P.: Fused Alumina Production. The Metallurgical Society of the American Institute of Mining, Metallurgical, and Petroleum Engineers, Paper No. EFC-7, New York, 48 pp., 1972.

Cliff, G. and Lorimer, G.W.: The quantitative analysis of thin specimens, J. Microscopy, 103, 203–207, https://doi.org/10.1111/j.1365-2818.1975.tb03895.x, 1975.

Coes, L. J.: Abrasives, Applied Mineralogy, vol. 1, Springer-Verlag, Wien, 177 pp., https://doi.org/10.1002/maco.19720230421, 1971.

Corrigan, F. R. and Bundy, F. P.: Direct transitions among the allotropic forms of boron nitride at high pressures and temperatures, J. Chem. Phys., 63, 3812–3820, 1975.

Cotter, P. G., Kohn, J. A., and Potter, R. A.: Physical and X-ray study of the disilicides of titanium zirconium, and hafnium, J. Am. Ceram. Soc., 39, 11-12, https://doi.org/10.1111-/j.1151-2916.1956.tb15590.x, 1956.

Davis, G. L. and Tuttle, O. F.: Two new crystalline phases of the anorthite composition, $CaO{\cdot}Al_2O_3{\cdot}2SiO_2$, Am. J. Sci., Bowen Volume, 107–114, 1952.

Day, H. W.: A revised diamond-graphite transition curve, Am. Mineral., 97, 53–62, 2012.

Dobrzhinetskaya, L. F., Wirth, R., Yang, J., Hutcheon, I. D., Weber, P. K., and Green II., H. W.: High-pressure highly reduced nitrides and oxides from chromitite of a Tibetan ophiolite, P. Natl. Acad. Sci. USA, 106, 19233–19238, https://doi.org/10.1073/pnas.0905514106, 2009

Dobrzhinetskaya, L. F., Wirth, R., Yang, J., Green, H. W., Hutcheon, I. D., Weber, P. K., and Grew, E. S.: Qingsongite, natural cubic boron nitride: The first boron mineral from the Earth's mantle, Am. Mineral., 99, 764–772, https://doi.org/10.2138/am.2014.4714, 2014.

Essene, E. J. and Fisher, D. C.: Lightning Strike Fusion: Extreme Reduction and Metal-Silicate Liquid Immiscibility, Science, 234, 189–193, https://doi.org/10.1126/science.234.4773.189, 1986.

Evans, N. J., Davis, J. J., Byrnec, J. P., and French, D.: Contamination-free preparation of geological samples for ultra-trace gold and platinum-group element analysis, J. Geochem. Exp. 80, 19–24, https://doi.org/10.1016/S0375-6742(03)00140-7, 2003.

Fahey, J. A., Weber, W. J., and Rotella, F. J.: An X-Ray and neutron powder diffraction study of the

$Ca_{2+x}Nd_{8-x}(SiO_4)_6O_{2-0.5x}$ system, J. Solid State Chem., 60, 145–158, https://doi.org/10.1016/0022-4596(85)90106-9, 1985.

Fang, Q. S., Bai, W. J., Yang, J. S., Xu, X. Z., Li, G. W., Shi, N. C., Xiong, M., and Rong, H.: Qusongite (WC): A new mineral, Am. Mineral., 94, 387–390, https://doi.org/10.2138/am.2009.3015, 2009.

Fang, Q., Bai, W., Yang, J., Rong, H., Shi, N., Li, G., Xiong, M., and Ma, Z.: Titanium, Ti, a new mineral species from Luobusha, Tibet, China, Act. Geol. Sin. 87, 1275–1280, https://doi.org/10.1111/1755-6724.12128, 2013.

Filonenko, N. E. and Lavrov, I. V.: Petrography of the Artificial Abrasives, Mashgiz, Moscow, 90 pp., 1958 (in Russian).

Fiore, M., Beneduce Netoa, F. B., and de Farias Azevedoa, C. R.: Assessment of the Ti-Rich corner of the Ti-Si phase diagram: The recent dispute about the eutectoid reaction, Mater. Res., 19, 942–953, https://doi.org/10.1590/1980-5373-MR-2016-0157, 2016.

Fisher, G.: Zirconia: Ceramic engineering's toughness challenge, Am. Ceram. Soc. Bull., 65, 1355–1360, 1986.

Frommeyer, G. and Rosenkranz, R.: Structures and properties of the refractory silicides Ti_5Si_3 and $TiSi_2$ and Ti-Si-(Al) eutectic alloys, in: Metallic Materials with High Structural Efficiency, edited by: Senkov, O. N., Miracle, D. B., and Firstov, S. A., NATO Science Series, Series II: Mathematics, Physics and Chemistry, 146, 287–308, https://doi.org/10.1007/1-4020-2112-7_30, 2004.

Gemmi, M. and Lanza, A.: 3D electron diffraction techniques, Acta Cryst., 75, 495–504, https://doi.org/10.1107/S2052520619007510, 2019.

Gemmi, M., Mugnaioli, E., Gorelik, T. E., Kolb, U., Palatinus, L., Boullay, P., Hovmöller, S., and Abrahams, J. P.: 3D electron diffraction: the nanocrystallography revolution, ACS Cent. Sci., 5, 1315–1329, https://doi.org/10.1021/acscentsci.9b00394, 2019.

Gewecke, J.: Ueber die Phosphide des Titans and Zirkons, Liebigs Ann. Chem., 361, 79–88, https://doi.org/10.1002/jlac.19083610106, 1908.

Goldsmith, J. R.: The melting and breakdown reactions of anorthite at high pressures and temperatures, Am. Mineral., 65, 272–284, https://doi.org/10.1007/BF01243532, 1980.

Griffin, W. L., Gain, S. E. M., Adams, D. T., Huang, J. X., Saunders, M., Toledo, V., Pearson, N. J., and O'Reilly, S. Y.: First terrestrial occurrence of tistarite (Ti_2O_3): Ultra-low oxygen fugacity in the upper mantle beneath Mount Carmel, Israel, Geology, 44, 815–818, https://doi.org/10.1130/G37910.1, 2016a.

Griffin, W. L., Afonso, J. C., Belousova, E. A., Gain, S. E., Gong, X.-H., González-Jiménez, J. M., Howell, D., Huang, J.-X., McGowan, N., Pearson, N. J., Satsukawa, T., Shi, R.,Williams, P., Xiong, Q., Yang, J.-S., Zhang, M., and O'Reilly, S. Y.: Mantle recycling: transition-zone metamorphism of Tibetan ophiolitic peridotites and its tectonic implications, J. Petrol., 57, 655–684 https://doi.org/10.1093/petrology/egw011, 2016b.

Griffin, W. L., Huang, J.-X., Thomassot, E., Gain, S. E. M., Toledo, V., and O'Reilly, S. Y.: Super-reducing conditions in ancient and modern volcanic systems: Sources and behaviour of carbon-rich fluids in the lithospheric mantle, Mineral. Petrol., 112, 101–114, https://doi.org/10.1007/s00710-018-0575-x, 2018.

Griffin, W. L., Gain, S. E., Huang, J.-X., Saunders, M., Shaw, J., Toledo, V., and O'Reilly, S. Y.: A terrestrial magmatic hibonite-grossite-vanadium assemblage: desilication and extreme reduction in a volcanic plumbing system, Mount Carmel, Israel, Am. Mineral. 104, 207–219, https://doi.org/10.2138/am-2019-6733, 2019a.

Griffin, W. L., Toledo, V., and O'Reilly, S. Y.: Discussion of "Enigmatic super-reduced phases in corundum from natural rocks: possible contamination from artificial abrasive materials or metallurgical slags" by Litasov et al., (Lithos, v.340–341, p.181–190), Lithos, 348, 105122, https://doi.org/10.1016/j.lithos.2019.06.024, 2019b.

Griffin, W. L., Gain, S. E. M., Saunders, M., Bindi, L., Alard, O., Toledo, V., and O'Reilly, S. Y.: Parageneses of TiB_2 in corundum xenoliths from Mt Carmel, Israel: Siderophile behaviour of boron under reducing conditions, Am. Mineral., https://doi.org/10.2138/am-2020-7375, in press, 2020.

Hariya, Y. and Kennedy, G. C.: Equilibrium study of anorthite under high pressure and high temperature, Am. J. Sci., 266, 193–203, https://doi.org/10.2475/ajs.266.3.193, 1968.

Hawthorne, F. C., Burke, E. A. J., Ercit, T. S., Grew, E. S., Grice, J. D., Jambor, J. L., Puziewicz, J., Roberts, A. C., and Vanko, D. A.: New Mineral Names, Am. Mineral., 73, 189–199, 1988.

Hönigschmid, O.: Surle siliciure de zirconium $ZrSi_2$ et le siliciure de titane $TiSi_2$, Cr. Hebd. Acad. Sci., 143, 224–226, 1906.

Jeitschko, W.: Refinement of the crystal structure of $TiSi_2$ and some comments on bonding in $TiSi_2$ and related compounds, Act. Crystallogr., B33, 2347–2348, https://doi.org/10.1107/S0567740877008462, 1977.

Knausenberger, M., Brauer, G., and Gingerich, K. A.: Preparation and phase studies of titanium phosphides, J. Less-Common Met., 8, 136–148, https://doi.org/10.1016/0022-5088(65)90105-0, 1965.

Kolb, U., Mugnaioli, E., and Gorelik, T. E.: Automated electron diffraction tomography – A new tool for nano crystal structure analysis, Cryst. Res. Technol., 46, 542–554, https://doi.org/10.1002/crat.201100036, 2011

Krivovichev, S. V., Shcherbakova, E. P., and Nishanbaev, T. P.: The crystal structure of svyatoslavite and evolution of complexity during crystallization of a $CaAl_2Si_2O_8$ melt: A structural automata description, Can. Mineral., 50, 585–592, https://doi.org/10.3749/canmin.50.3.585, 2012.

Laves, F. and Wallbaum, H. J.: Die Kristallstruktur von Ni_3Ti und Si_2Ti, Z. Kristallogr., 101, 78–93, https://doi.org/10.1524/zkri.1939.101.1.78, 1939.

Li, C. Y., Yu, Z. H., Liu, H. Z., and Lü, T. Q.: The crystallographic stability and anisotropic compressibility of C54- type $TiSi_2$ under high pressure, J. Phys. Chem. Sol., 74, 1291–1294, https://doi.org/10.1016/j.jpcs.2013.04.006, 2013.

Li, G., Fang, Q., Shi, N., Bai, W., Yang, J., Xiong, M., Ma, Z., and Rong, H.: Zangboite, $TiFeSi_2$, a new mineral species from Luobusha, Tibet, China, and its crystal structure, Can. Mineral., 47, 1265–1274, https://doi.org/10.3749/canmin.47.5.1265, 2009.

Li, G., Bai, W., Shi, N., Fang, Q., Xiong, M., Yang, J., Ma, Z., and Rong, H.: Linzhiite, $FeSi_2$, a redefined and revalidated new mineral species from Luobusha, Tibet, China, Eur. J. Mineral., 24, 1047–1052, https://doi.org/10.1127/0935-1221/2012/0024-2237, 2012.

Liang, F., Xu, Z., and Zhao, J.: In-situ moissanite in dunite of the Luobusa Ophiolite, Tibet: Implications for deep mantle origin,

Acta Geol. Sin.-Engl., 89, 47–49, https://doi.org/10.1111/1755-6724.12308_32, 2015.

Litasov, K. D., Kagi, H., and Bekker, T. B.: Enigmatic super-reduced phases in corundum from natural rocks: Possible contamination from artificial abrasive materials or metallurgical slags, Lithos, 340–341, 181–190, https://doi.org/10.1016/j.lithos.2019.05.013, 2019a.

Litasov, K. D., Bekker, T. B., and Kagi, H.: Reply to the discussion of "Enigmatic super-reduced phases in corundum from natural rocks: Possible contamination from artificial abrasive materials or metallurgical slags" by Litasov et al. (Lithos, v.340–341, p.181–190) by W.L. Griffin, V. Toledo and S.Y. O'Reilly, Lithos, 348–349, 105170, https://doi.org/10.1016/j.lithos.2019.105170, 2019b.

Liu, J. and Ownby, P. D.: Enhanced mechanical properties of alumina by dispersed titanium diboride particulate inclusions, J. Am. Ceram. Soc., 74, 241–243, https://doi.org/10.1111/j.1151-2916.1991.tb07327.x, 1991.

Lundström, T.: Preparation and crystal chemistry of some refractory borides and phosphides, Ark. Kemi, 31, 227–266, 1969.

Malpas, J., Zhou, M. F., Robinson, P. T., and Reynolds, P.: Geochemical and geochronological constraints on the origin and emplacement of the Yarlung-Zangbo ophiolites, Southern Tibet, in: Ophiolites Through Earth History, edited by: Dilek, Y. and Robinson, P. T., Geol. Soc. Sp., 218, 191–206, https://doi.org/10.1144/GSL.SP.2003.218.01.11, 2003.

Mohammad Sharifi, E., Karimzadeh, F., and Enayati, M. H.: Synthesis of titanium diboride reinforced alumina matrix nanocomposite by mechanochemical reaction of Al–TiO_2–B_2O_3, J. Alloy. Compd., 502, 508–512, https://doi.org/10.1016/j.jallcom.2010.04.207, 2010.

Momma, K. and Izumi, F.: VESTA 3 for three-dimensional visualization of crystal, volumetric and morphology data, J. Appl. Crystallogr., 44, 1272–1276, https://doi.org/10.1107/S0021889811038970, 2011.

Mugnaioli, E., Gorelik, T., and Kolb, U.: "Ab initio" structure solution from electron diffraction data obtained by a combination of automated diffraction tomography and precession technique, Ultramicroscopy, 109, 758–765, https://doi.org/10.1016/j.ultramic.2009.01.011, 2009.

Nederlof, I., van Genderen, E., Li, Y., and Abrahams, J. P.: A Medipix quantum area detector allows rotation electron diffraction data collection from submicrometre three-dimensional protein crystals, Act. Crystallogr. D, 69, 1223–1230, https://doi.org/10.1107/S0907444913009700, 2013.

Nowotny, H.: Alloy chemistry of transition elements borides, carbites, nitrides, aluminides, and silicides, in Electronic structure and Alloy Chemistry of the Transition Elements, edited by: Beck, P. A., Wiley & Sons, New York, London, 179–220, 1963.

Ohtani, H., Hanaya, N., Hasebe, M., Teraoka, S., and Abe, M.: Thermodynamic Analysis of the Fe-Ti–P Ternary System by Incorporating First-Principles Calculations into the CALPHAD Approach, Calphad, 30, 147–158, https://doi.org/10.1016/j.calphad.2005.09.006, 2006.

Okamoto, H.: P-Ti (Phosphorus-Titanium), J. Phase Equilib. Diff., 28, 587, https://doi.org/10.1007/s11669-007-9184-9, 2007.

Ottonello, G., Attene, M., Ameglio, D., Belmonte,D., Zuccolini, M. V., and Natali, M.: Thermodynamic investigation of the CaO–Al_2O_3–SiO_2 system at high P and T through polymer chemistry and convex-hull techniques, Chem. Geol., 346, 81–92, https://doi.org/10.1016/j.chemgeo.2012.09.018, 2013.

Palatinus, L., Petříček, V., and Correa, C. A.: Structure refinement using precession electron diffraction tomography and dynamical diffraction: theory and implementation, Act. Crystallogr. A, 71, 235–244, https://doi.org/10.1107/S2053273315001266, 2015.

Palatinus, L, Brázda, P., Jelínek, M., Hrdá, J., Steciuk, G., and Klementová, M.: Specifics of the data processing of precession electron diffraction tomography data and their implementation in the program PETS2.0, Acta Crystallogr., 75, 512–522, 2019.

Pekov, I. V., Anikin, L. P., Chukanov, N. V., Belakovskiy, D. I., Yapaskurt, V. O., Sidorov, E. G., Britvin, S. N., and Zubkova, N. V.: Deltalumite, a new natural modification of alumina with spinel-type structure, Zapiski Rossiiskogo Mineralogicheskogo Obshchetstva 148, 45–58, 2019 (in Russian).

Peshov, P. and Kristov, M.: Preparation of titanium disilicide single crystals by chemical vapour transport with halogens, J. Less-Common Met., 117, 361–368, https://doi.org/10.1016/0022-5088(86)90061-5, 1986.

Petříček, V., Dušek, M., and Palatinus, L.: Crystallographic computing system JANA2006: general features, Z. Kristallogr., 229, 345–352, https://doi.org/10.1515/zkri-2014-1737, 2014.

Polubelova, A. S., Krylov, V. N., Karlin, V. V., and Efimova, I. S.: Production of Abrasive Materials, Mashinostroenie, Leningrad, 1968 (in Russian).

Ripley, R. L.: The preparation and properties of some transition phosphides, J. Less-Common Met., 4, 496–503, https://doi.org/10.1016/0022-5088(62)90037-1, 1962.

Robinson, P. T., Bai, W.-J., Malpas, J., Yang, J.-S., Zhou, M.-F., Fang, Q.-S., Hu, X.-F., and Cameron, S.: Ultra-high pressure minerals in the Luobusha ophiolite, Tibet and their tectonic implications, in: Aspects of the tectonic evolution of China, edited by: Malpas, J., Fletcher, C. J. N., Ali, J. R., and Aitchison, J. C., Geol. Soc. Sp., 226, 247–271, https://doi.org/10.1144/GSL.SP.2004.226.01.14, 2004.

Robinson, P. T., Trumbull, R. B., Schmitt, A., Yang, J. S., Li, J. W., Zhou, M. F., Erzinger, J., Dare, S., and Xiong, F. H.: The origin and significance of crustal minerals in ophiolitic chromitites and peridotites, Gondwana Res., 27, 486–506, https://doi.org/10.1016/j.gr.2014.06.003, 2015.

Ross, A. J., Downes, H., Herrin, J. S., Mittlefehldt, D. W., Humayun, M., and Smith, C.: The origin of iron silicides in ureilite meteorites, Geochemistry, 79, 125539, https://doi.org/10.1016/j.chemer.2019.125539, 2019.

Schrewelius, N. G.: Constitution and microhardness of fused corundum abrasives, J. Am. Ceram. Soc., 31, 170–175, https://doi.org/10.1111/j.1151-2916.1948.tb14285.x, 1948.

Shi, N. C., Bai, W. J., Li, G. W., Xiong, M., Yang, J. S., Ma, Z. S., and Rong, H.: Naquite, FeSi, a new mineral species from Luobusha, Tibet, Western China, Act. Geol. Sin., 86, 533–538, https://doi.org/10.1111/j.1755-6724.2012.00682.x, 2012.

Snell, P.-O.: The crystal structure of TiP, Act. Chem. Scand., 27, 1773–1776, https://doi.org/10.3891/acta.chem.scand.21-1773, 1967.

Stubicon, V. S. and Hellmann, J. R.: Phase equilibria in some zirconia systems, Science and Technology of Zirconia, 25–36, 1981.

Su, B., Zhou, M., Jing, J., Robinson, P. T., Chen, C., Xiao, Y., Xia Liu, X., Shi, R., Davide Lenaz, D., and Hu, Y.: Distinctive melt activity and chromite mineralization in Luobusa and Pu-

rang ophiolites, southern Tibet: constraints from trace element compositions of chromite and olivine, Sci. Bull., 64, 108–121, https://doi.org/10.1016/j.scib.2018.12.018, 2019.

Sun, Y., Li, Y., Zhang, L., Shen, Y., and Sun, J.: Formation mechanism of Ti(C, N) solid solution in Al-brown fused alumina refractory at 1973 K in flowing N2, Ceramics International, 46, 2654–2660, https://doi.org/10.1016/j.ceramint.2019.09.250, 2020.

Svechnikov, V. N., Kocherzhisky, Y. A., Yupko, L. M., Kulik, O. G., and Shinshkin, E.A.: Phase diagram of the titanium-silicon system, Doklady Akademii Nauk SSSR, 193, 393–396, 1970 (in Russian).

Takéuchi, Y. and Donnay, G.: The crystal structure of hexagonal $CaAl_2Si_2O_8$, Acta Crystallogr, 12, 465–470, https://doi.org/10.1107/S0365110X59001396, 1959.

Ulmer, G. C., Grandstaff, D. E., Woermann, E., Göbbels, M., Schönitz, and Woodland, A. B.: The redox stability of moissanite (SiC) compared with metal-metal oxide buffers at 1773 K and at pressures up to 90kbar, Neues Jahrbuch für Mineralogie – Abhandlungen, 172, 279–307, 1998.

Utsunomiya, S., Yudintsev, S., Wang, L. M., and Ewing, R. C.: Ion-beam and electron-beam irradiation of synthetic britholite, J. Nucl. Mater., 322, 180–188, https://doi.org/10.1016/S0022-3115(03)00327-1, 2003.

Vincent, R. and Midgley, P. A.: Double conical beam-rocking system for measurement of integrated electron diffraction intensities, Ultramicroscopy, 53, 271–282, https://doi.org/10.1016/0304-3991(94)90039-6, 1994.

Wang, H. S., Bai, W. J., Wang, B. X., and Chai, Y. C.: Chromite deposits in China and their origin, Beijing: Science Publishing House, 1983 (in Chinese).

Wang, X. B., Bao, P. S., Deng, W. M., and Wang, F. G.: Tibet ophiolite, Beijing: Geological Publishing House, 1987 (in Chinese).

Wang, X. B., Zhou, X., and Hao, Z. G.: Some opinions on further exploration for chromite deposits in the Luobusa area, Tibet, China, Geol. Bull. China, 29, 105–114, 2010 (in Chinese with English abstract).

Weitzer, F., Schuster, J. C., Naka, M., Stein, F., and Pulm, M.: On the reaction scheme and liquidus surface in the ternary system Fe–Si–Ti, Intermetallics, 16, 273–282, https://doi.org/10.1016/j.intermet.2007.10.006, 2008.

Wirth, R.: Focused ion beam (FIB): a novel technology for advanced application of micro- and nanoanalysis in geosciences and applied mineralogy, Eur. J. Mineral., 16, 863–877, https://doi.org/10.1127/0935-1221/2004/0016-0863, 2004.

Wirth, R.: Focused ion beam (FIB) combined with SEM and TEM: advanced analytical tools for studies of chemical composition, microstructure and crystal structure in geomaterials on a nanometre scale, Chem. Geol., 261, 217–229, https://doi.org/10.1016/j.chemgeo.2008.05.019, 2009.

Xiong, F. H., Yang, J. S., Robinson, P. T., Xu, X. Z., Liu, Z., Li, Y., Liu, F., and Chen, S. Y.: Origin of podiform chromitite, a new model based on the Luobusha ophiolite, Tibet, Gondwana Res., 27, 525–542, https://doi.org/10.1016/j.gr.2014.04.008, 2015.

Xiong, F., Xu, X., Mugnaioli, E., Gemmi, M., Wirth, R., Grew, E. S., and Robinson, P. T.: Potential new titanium minerals in corundum from the Cr-11 chromitite orebody, Luobusa ophiolite, Tibet, China: Evidence for super-reduced mantle derived fluids?, Geol. Soc. Am., 51, 5, https://doi.org/10.1130/abs/2019AM-333493, 2019a.

Xiong, F. H., Xu, X. Z., Mugnaioli, E., Gemmi, M., Wirth, R., Grew, E. S., and Robinson, P. T.: Jingsuiite, IMA 2018-117b, in: New minerals and nomenclature modifications approved in 2019, edited by: Miyawaki, R., Hatert, F., Pasero, M. and Mills, S. J., CNMNC Newsletter No. 52, Mineralogical Magazine, 83, 887–893, https://doi.org/10.1180/mgm.2019.73, 2019b.

Xiong, F. H., Xu, X. Z., Mugnaioli, E., Gemmi, M., Wirth, R., Grew, E., and Robinson, P. T.: Badengzhuite, IMA 2019-076, in: New minerals and nomenclature modifications approved in 2019, edited by: Miyawaki, R., Hatert, F., Pasero, M. and Mills, S. J., CNMNC Newsletter No. 52, Mineralogical Magazine, 83, 887–893, https://doi.org/10.1180/mgm.2019.73, 2019c.

Xiong, F. H., Xu, X.Z., Mugnaioli, E., Gemmi, M., Wirth, R., Grew, E., and Robinson, P. T.: Zhiqinite, IMA 2019-077, in: New minerals and nomenclature modifications approved in 2019, edited by: Miyawaki, R., Hatert, F., Pasero, M. and Mills, S. J., CNMNC Newsletter No. 52, Mineralogical Magazine, 83, 887–893, https://doi.org/10.1180/mgm.2019.73, 2019d.

Xiong, F. H., Xu, X. Z., Mugnaioli, E., Gemmi, M., Wirth, R., and Grew, E. S.: $(K,Sr_{box})(Ca,_{box})_3Al_6Si_{10}O_{32}$, a dmisteinbergite-like phase from the Luobusa ophiolite, China: Evidence for quenching at mantle depths?, Goldschmidt Abstracts, 2928, 2020a.

Xiong, F. H., Xu, X. Z., Mugnaioli, E., Gemmi, M., Wirth, R., and Grew, E. S.: $Ti_{10}(Si,P)_{6-7}$ and $Ti_{11}(Si,P)_{10}$, new phases from the Luobusa ophiolite, China: Implications for crystallization of Ti-Si-P melts, Goldschmidt Abstracts, 2929, 2020b.

Xiong, F., Xu, X., Mugnaioli, E., Gemmi, M., Wirth, R., Grew, E.S. and Robinson, P. T.: Jingsuiite, TiB_2, a new mineral from the Cr-11 podiform chromitite orebody, Luobusa ophiolite, Tibet, China: Implications for recycling of boron, Am. Mineral., submitted, 2020c.

Xiong, Q., Griffin, W. L., Huang, J.-X., Gain, S. E. M., Toledo, V., Pearson, N. J., and O'Reilly, S. Y.: Super-reduced mineral assemblages in "ophiolitic" chromitites and peridotites: the view from Mount Carmel, Eur. J. Mineral., 29, 557–570, https://doi.org/10.1127/ejm/2017/0029-2646, 2017.

Xu, X., Yang, J., Chen, S., Fang, Q., and Bai, W.: Unusual Mantle Mineral Group from Chromitite Orebody Cr-11 in Luobusha Ophiolite of Yarlung-Zangbo Suture Zone, Tibet, J. Earth Sci., 20, 284–302, https://doi.org/10.1007/s12583-009-0026-z, 2009.

Xu, X. Z., Yang, J. S., Guo, G. L., and Xiong, F. H.: Mineral inclusions in corundum from chromitites in the Kangjinla chromite deposit, Tibet, Act. Petrol. Sin., 29, 1867–1877, 2013 (in Chinese with English abstract).

Xu, X. Z., Yang, J. S., Robinson, P. T., Xiong, F. H., Ba, D. Z., and Guo, G. L.: Origin of ultrahigh pressure and highly reduced minerals in podiform chromitites and associated mantle peridotites of the Luobusha ophiolite, Tibet, Gondwana Res., 27, 686–700, https://doi.org/10.1016/j.gr.2014.05.010, 2015.

Xu, X. Z., Yang, J. S., Xiong, F. H., and Guo, G. L.: Characteristics of titanium-bearing inclusions found in corundum of Luobusha podiform chromitite, Tibet, Earth Sci., 43, 1025–1037, 2018 (in Chinese with English abstract).

Xu, Z. Q., Dilek, Y., Yang, J. S., Liang, H. F., Liu, F., Ba, D. Z., Cai, Z. H., Li, G. W., Dong, H. W., and Ji, S. C.: Crustal structure of the Indus–Tsangpo suture and its ophiolites in southern Tibet, Gondwana Res., 27, 507–524, https://doi.org/10.1016/j.gr.2014.08.001, 2014.

Yamamoto, H., Yamamoto, S., Kaneko, Y.,Terabayashi, M., Komiya, T., Katayama, I., and Iizuka, T.: Imbricate structure of the Luobusa Ophiolite and surrounding rock units, southern Tibet, J. Asian Earth Sci., 29, 296–304, https://doi.org/10.1016/j.jseaes.2006.04.004, 2007.

Yang, J. S., Bai, W. J., Fang, Q. S., Yan, B. G., Shi, N. C., Ma, Z. S., Dai, M. Q., and Xiong, M.: Silicon-rutile – an ultrahigh pressure (UHP) mineral from an ophiolite, Progr. Nat. Sci., 13, 528–531, 2003.

Yang, J. S., Bai, W. J., Fang, Q. S., Yan, B. G., Rong, H., and Chen, S. Y.: Coesite discovered from the podiform chromitite in the Luobusa ophiolite, Tibet, Earth Science, J. China Univ. Geosci., 29, 651–660, https://doi.org/10.1007/BF02873097, 2004.

Yang, J.-S., Dobrzhinetskaya, L., Bai, W. J., Fang, Q. S., Robinson, P. T., Zhang, J., and Green, H. W. II.: Diamond- and coesite-bearing chromitites from the Luobusa ophiolite, Tibet, Geology, 35, 875–878, https://doi.org/10.1130/G23766A.1, 2007.

Yang, J. S., Bai, W. J., Fang, Q. S., and Rong, H.: Ultrahigh-pressure minerals and new minerals from the Luobusa ophiolitic chromitites in Tibet: A review, Act. Geosci. Sin., 29, 263–274, 2008 (in Chinese).

Yang, J. S., Robinson, P. T., and Dilek, Y.: Diamond-bearing ophiolites and their geological occurrence, Episodes, 38, 344–364, https://doi.org/10.18814/epiiugs/2015/v38i4/82430, 2015.

Yu, Z.: Two new minerals gupeiite and xifengite in cosmic dusts from Yanshan, Acta Petrologica Mineralogica et Analytica 3, 231–238, 1984 (in Chinese with an English abstract).

Zhang, R.Y., Yang, J.S., Ernst, W. G., Jahn, B.-M., Lizuka, Y., and Guo, G.L.: Discovery of in situ super-reducing, ultrahigh-pressure phases in the Luobusha ophiolitic chromitites, Tibet: New insights into the deep upper mantle and mantle transition zone, Am. Mineral., 101, 1285–1294, https://doi.org/10.2138/am-2016-5436, 2016.

Zhou, M. F., Robinson, P. T., Malpas, J., and Li, Z.: Podiform chromitites in the Luobusa Ophiolite (southern Tibet): implications for melt–rock interaction and chromite segregation in the upper mantle, J. Petrol., 37, 3–21, https://doi.org/10.1093/petrology/37.1.3, 1996.

Zolotarev, A .A., Krivovichev, S. V., Panikorovskii, T. L., Gurzhiy, V. V., Bocharov, V. N., and Rassomakhin, M. A.: Dmisteinbergite, $CaAl_2Si_2O_8$, a Metastable Polymorph of Anorthite: Crystal-Structure and Raman Spectroscopic Study of the Holotype Specimen, Minerals, 9, 570, https://doi.org/10.3390/min9100570, 2019.